Direct Numerical Simulation of Bubble Formation through a Submerged "Flute"

Naveen Pillai [1]
Department of Nuclear Engineering,
North Carolina State University
2500 Stinson Dr,
Raleigh, NC
27607

npillai2@ncsu.edu

Nicholas Sponsel
Department of Nuclear Engineering,
North Carolina State University
2500 Stinson Dr,
Raleigh, NC
27607

nlsponse@ncsu.edu

Katharina Stapelmann
Department of Nuclear Engineering,
North Carolina State University
2500 Stinson Dr,
Raleigh, NC
27607

kstapel@ncsu.edu

Igor A. Bolotnov
Department of Nuclear Engineering,
North Carolina State University
2500 Stinson Dr,
Raleigh, NC
27607

iabolotn@ncsu.edu

---

[1] Corresponding author

ABSTRACT

Direct Numerical Simulation (DNS) is often used to uncover and highlight physical phenomena that are not properly resolved using other Computational Fluid Dynamics (CFD) methods due to shortcuts taken in the latter to cheapen the computational cost. In this work, we use DNS along with interface tracking to take an in-depth look at bubble formation, departure, and ascent through water. To form the bubbles, air is injected through a novel orifice geometry not unlike that of a flute submerged underwater, which introduces phenomena that are brought to light in conventional orifice studies. For example, our single-phase simulations show a significant leaning effect wherein pressure accumulating at the trailing nozzle edges leads to asymmetric discharge through the nozzle hole, and an upward bias in the flow in the rest of the pipe. In our two-phase simulations, this effect is masked by the surface tension of the bubble sitting on the nozzle but can still be seen following departure events. After bubble departure, we see the bubbles drift rapidly toward an ellipsoidal shape, which has been validated using experiments. As the bubbles rise, we note that local variations in vertical velocity component cause the bubble edges to flap slightly, oscillating between relatively low and high velocities at the edges, causing them to respectively lag and lead the bulk bubble mass.

1 INTRODUCTION

There is a large body of work investigating two phase flow through submerged orifices, both experimentally [1–8], and computationally [9–12]. However, all known cases involve air inflow perpendicular to the plane of the orifice, typically vertical air injections into a small chamber blocked off by a plate with a hole (orifice) drilled into it. This geometry has a significant array of applications in industry, such as in bubble columns and slurry reactors. While there are some studies with air inflow into moving water [3,6], there is a lack of research done with air cross-flow into stagnant water.

Furthermore, research done on orifice flows often focus on orifices larger than 1 mm in diameter, though there are exceptions [2,3,6,8,12]. We note a few reasons for this: i) the difficulty in precisely drilling sub-millimeter orifices is a barrier to performing this experimentally; even if such orifices could be machined, they would restrict bulk flow by a large amount unless used in large numbers relative to the plate area, which would inherently entangle the dynamics of each orifice to those adjacent to it – limiting the scope of such studies to measuring bulk quantities [7]; ii) it is very difficult to experimentally capture accurate two-phase information such as the bubble shape/volume/location at sub-millimeter scales without significantly compromising bubble integrity iii) the quality of computational fluid dynamics (CFD) codes with interface tracking has only recently reached the point wherein such simulations can be performed – these emergent capabilities have been first utilized to gain new insight into existing problems, rather than as a tool to uncover novel scientific insights. Simmons et al. [12] reviewed the progression of research in underwater bubble formation spanning 40 years, and noted that at the time (2015), for a millimeter-sized bubble, experiments were able to capture and resolve pictures down to tens of microns, whilst “numerical methods have thus far failed to capture [those] scales” [12]. In their discussion, they did not mention any 3-D computational approach, so it is not surprising that the cited numerical methods failed to aptly capture and resolve continuum mechanics at those scales. Moreover, the real issue herein is not absolute scale resolution, but the dynamic range of scales resolved in a cohesive dataset, whether through simulations or experiments. By just using a local cluster (up to 640 processing cores, with typical runs using 256 cores), we have been able to capture phenomena spanning three orders of magnitude – from tens of microns (at the orifice) to centimeters above the orifice, and with modern supercomputing, we have the capability to capture phenomena spanning four orders of magnitude. For example, work by Fang et al. [13] studied bubbly flow with over 600 sub-millimeter sized bubbles in a subchannel 10 centimeters long and a bulk mesh size of 30 microns using simulations run on the Argonne Leadership Computing Facility (ALCF) machine “Mira” – which was built in 2012 and was #3 fastest supercomputer in the world at that time.

Past experimental studies have almost exclusively examined orifices drilled into flat surfaces [1,3–8] as this is not only much easier to manufacture, but also fitting for conventional applications. Past numerical studies [9–12] have ignored behavior below the orifice, starting the computational domain at the orifice opening – unlike our domain, which includes a well resolved region below the orifice. One study by Qu et al. [2] used very thin submerged pipes (with inner diameters ranging from 0.11 mm to 0.24 mm). Though these pipes were referred to as “micro-orifices” by the authors, it is unclear to what extent the dynamics of bubble formation observed therein would be comparable to that of a traditional orifice, where all the inflow does not directly reach the orifice, instead of causing air recirculation in the corners furthest from the opening (see Fig. 1). However, laminar flow in the thin pipe configuration may produce results similar to our air cross-flow configuration wherein we also expect no recirculation due to the opportunity for the air to exit at the next orifice. We expect similar liquid recirculation behavior, particularly as a bubble departs, but the authors in [2] did not look into this aspect of bubble formation.

Our work simultaneously introduces three novel variations to the conventional orifice problem: i) air cross-flow, wherein the air inflow is parallel to the plane of each orifice; ii) small orifices, each orifice in this investigation has a diameter of 0.5 mm; iii) a cylindrical orifice exterior, while this is largely a challenge for experimentalists, especially with orifices of this scale, the curved surface could impact certain dynamics of bubble formation, such as the local liquid flow around bubbles as they form. This work aims to break new ground using direct numerical simulation (DNS) to uncover intricate, small-scale fluid dynamics that occur in this novel orifice geometry.

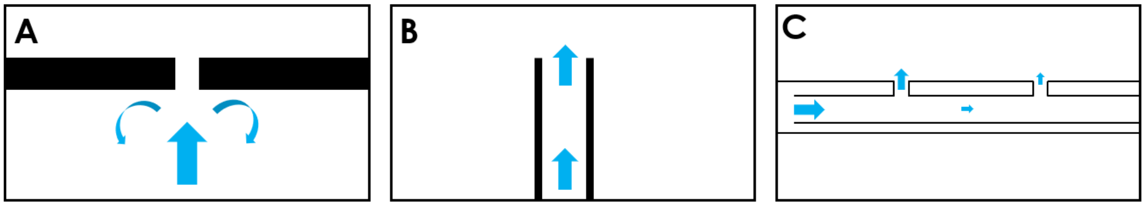

Fig. 1 *Various orifice configurations:* ***A.*** *Conventional plate orifice* ***B.*** *Thin pipe as seen in [2]* ***C.*** *Our configuration with air cross-flow.*

1.1 Background

The apparatus introduced here is a setup designed to efficiently treat water with non-thermal plasma. Plasma-water treatment has been of increasing interest for various applications, e.g. as a novel method to produce fertilizer from water and air [14], or for the decomposition of contaminants in water, such as polyfluoroalkyl substances (PFAS) [15], or pharmaceutical residuents [16]. The direct ignition of plasma in liquids is difficult to achieve due to the large magnitude of electric field required – that which supersedes practical limitations [17,18]. Stratton et al. [19] investigated the efficiency of different plasma reactor concepts and found that the surface to volume ratio plays a major role for the efficiency of plasma-based degradation of contaminants. Reactive species produced by the plasma enter the liquid to react further with contaminants or to accumulate as nitrates and nitrites, for example, in the case of plasma agriculture. By increasing the volume to surface ratio, the transport of reactive species from the gaseous plasma phase into the liquid can be increased. One possibility to achieve that is the introduction of gas bubbles into the liquid. If a high voltage is applied to the bubble liquid mixture, a plasma can be ignited in the bubbles. Computational investigations have shown that streamer breakdown could occur in submerged bubbles of a much lower density (and higher permittivity) than that of the surrounding fluid, such as air [20,21]. Prior studies have shown that due to the difference in permittivity between water and air, an electric field applied across a submerged bubble will be enhanced [20]. In addition, when an electric field is applied across ellipsoidal bubbles with the longest axis parallel to field lines (see

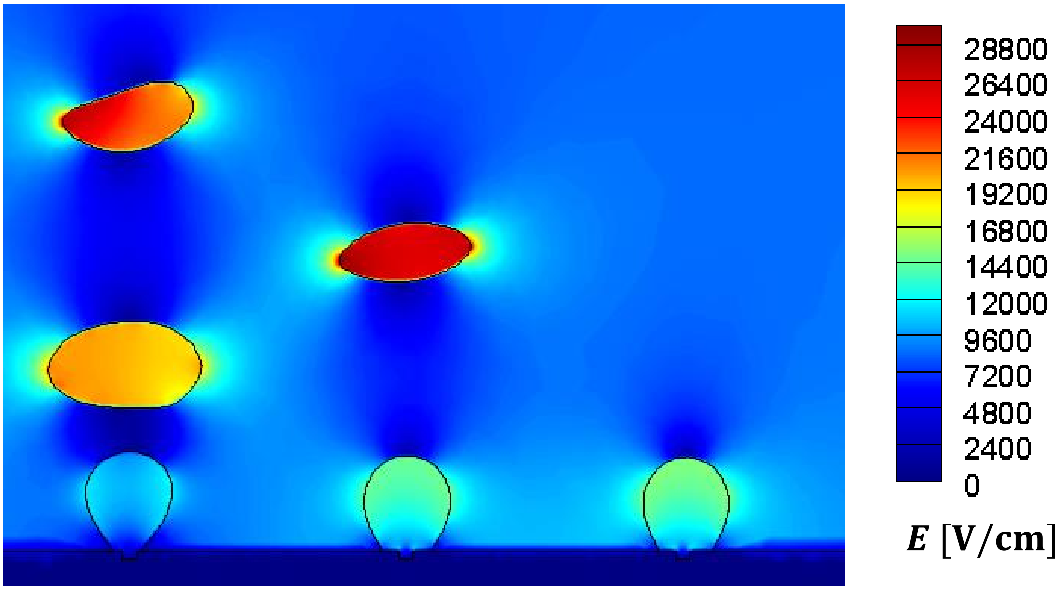

Fig. 2 *Electric field concentration in bubbles due to permittivity differences and proximity effects of adjacent bubbles.*

Fig. 2), the field is even further enhanced when compared to that which would be achieved with a spherical bubble of the same volume [21].

Computationally, resolving the liquid-gas interface exposed to an electric field is challenging. As identified in the Plasma-Liquid Roadmap (2016) “simulation of liquid-gas interfacial flows is a significant challenge due to the evolving, non-regular shapes and moving boundaries across which density changes by several orders of magnitude.” Small deformations which may be caused by the electric field and the required accuracy of interface tracking complicate the implementation. Turbulence is typically not included in plasma-liquid interaction models. DNS or large-eddy simulations are required to address the periodic motion occurring at the plasma-liquid interface, which has not been addressed by the community. The typical non-thermal, non-equilibrium plasmas are often described by de-coupled approaches which works well in most cases [22–24].

Sophisticated 3D models coupling computational fluid dynamics (CFD), electromagnetics, plasma-surface interactions, and mixture-dependent thermodynamics have been developed for thermal plasmas [25–27]. Computational fluid dynamics with fluid dynamic-thermal-electromagnetic coupling have mostly been applied for high-power plasma discharges which are or are close to (local) thermal equilibrium [28], for example the CFD simulation of radio-frequency plasma torches or the 3D simulation of electric welding [29,30]. Other CFD fluid models, such as nonPDPSIM [31], are limited to 2D where the interface between plasma and liquid is static, and relegates the problem to simple mass-transfer problem.

In many plasma-liquid interface models, the liquid is represented as a thin liquid layer [32–36], or as droplets [37] . The interface between plasma and liquid is treated as a mass-transfer problem. Limitations of the 2D approach can be observed when plasma is ignited in bubbles in liquids. The bubbles have been treated as an ideal ellipsoid [20,38,39] or elongated, compressed, and tilted [21]. Streamers in bubbles have similar physics to filaments in a DBD. A close proximity of the liquid-gas boundary with steep density and permittivity gradients causes surface-hugging streamers due to the refraction of the electric field along the surface of the bubble. Small bubbles lead to streamers that fill the whole bubble, since the streamer dimensions exceed the bubble dimensions. For larger bubbles, the plasma covers the bubble surface, forming a surface-hugging streamer, since the streamer dimensions are smaller than the bubble dimensions. It was also observed that the streamer path depends on the gas composition within the bubble. The performed simulations further indicate the possibility of transporting or communicating plasma streamers across multiple bubbles [40]. Overall, the shape and size of the bubble has been identified as an important parameter for plasma breakdown and formation. So far, realistic bubble shapes could not be studied computationally due to the truly 3-dimensional approach and the accuracy required for precise interface tracking.

1.2 Motivation

Multiphase systems with steep gradients consisting of plasma, gas, and liquid have gained interest for various applications, e.g. for water purification [16,19,41–43], for the production of fertilizer for plasma agriculture [44–50] or as plasma-treated liquids for medical applications [51–55]. The introduction of gas bubbles is of great interest because it i) lowers the electric field required for plasma breakdown, and ii) it opens another degree of freedom in this multiphase system that influences the plasma behavior. Furthermore, bubbles are ubiquitous in liquids, and additional bubbles can be produced throughout the liquid by energy transport at the plasma-liquid interface. Most of the plasma-bubble-liquid multiphase research focused on single bubble systems in a pin-to-plate geometry [56–58]. Both bubble shape and size were found to influence the breakdown and ignition behavior. Theoretical approaches have focused on ideal bubble shapes (ellipsoid) and have neglected three-dimensional realistic bubble shapes due to their complexity.

The experimental apparatus introduced here is a setup designed to efficiently treat water with plasma [44]. If a high voltage is applied to the bubble liquid mixture, a plasma can be ignited in the bubble. Computational investigations have shown that streamer breakdown could occur in submerged bubbles of a much lower density (and higher permittivity), such as air [20,21]. Prior studies have shown that due to the difference in permittivity between water and air, an electric field applied across a submerged bubble will be enhanced [20]. In addition, when an electric field is applied across ellipsoidal bubbles with the longest axis parallel to field lines (see Fig. 2), the field is even further enhanced when compared to that which would be achieved with a spherical bubble of the same volume [21].

Another trivial way to concentrate an electric field is by utilizing geometric attenuation in cylindrical geometry. Electrical field strength, like gravitational field strength, has an inverse square relationship with distance from a point source. If the point source were extended to a line source, the field strength would be inversely proportional to the distance from the source. We can use this relation to inform an experimental setup (described in Section 2.2), which forms the basis for the numerical setup described later in Section 2.2 & 2.3.

2 PROBLEM DESCRIPTION

2.1 Methodology

We have used a highly scalable and capable flow solver – PHASTA - to obtain the results in this work. PHASTA is a Parallel, Hierarchic, higher-order, Adaptive, Stabilized, Transient Analysis flow solver that is able to simulate incompressible flows in three dimensions on an unstructured grid using the finite element method (FEM). PHASTA has been used and validated in the study of various physical phenomena, such as: i) bubble formation through an injection port [10]; ii) bubble breakup [59,60]; iii) bubbly flows [61–

63]. Since our work will investigate very similar phenomena, i.e.: i) bubble formation through submerged orifices; ii) bubble detachment at these orifices; iii) bubbles rising through a stagnant fluid; PHASTA is an excellent choice for this study.

2.1.1 Governing Equations

DNS codes such as PHASTA directly solve for the strong form of the Incompressible Navier-Stokes equations (INS):

$$\nabla \cdot \underline{u} = 0 \tag{1}$$

$$\rho\left(\frac{\partial \underline{u}}{\partial t} + \underline{u} \cdot \nabla \underline{u}\right) = -\nabla \underline{P} + \nabla \cdot \underline{\underline{\tau}} + \underline{f} = 0$$
$$\underline{\underline{\tau}} = \mu\left(\nabla \underline{u} + \nabla \underline{u}^{T}\right) \tag{2}$$

The continuum surface tension model developed by Brackbill et. al [64] is used to compute the surface tension force as a volumetric force density smeared across the interfacial region (and included as a body force in Eq. 2). Further numerical details can be found in [65–67]

2.1.2 Level Set Method

We use the level-set method developed by Sussman et. al [68] and Sethian [69] to track the interface. This method utilizes a signed distance function (φ) to track the interface, where positive values of φ are indicative of the liquid phase and negative values of φ are indicative of the gas phase. The interface exists where φ=0, i.e. the zero level-set. The distance function is advected according to the following equation:

$$\frac{\partial \phi}{\partial t} + \underline{u} \cdot \nabla \phi = 0 \tag{3}$$

where $\underline{u}$ is the flow velocity vector.

As the distance function accounts for the presence of both liquid and gas, the INS equations are solved for only one fluid, whose properties such as density and viscosity, are smeared across the interface using a smoothed Heaviside function *H(φ)*. The value of any fluid property α is set as follows,

$$\alpha(\phi) = \alpha_1 H(\phi) + \alpha_2(1 - H(\phi)) \qquad (4)$$

where α_1 is the property value of the liquid and α_2 is the property value of the gas. The smoothed Heaviside function is defined according to the interface thickness, ε [68];

$$H(\phi) = \left\{ \begin{array}{cc} 0\,, & \phi < -\epsilon \\ \frac{1}{2}\left[1 + \frac{\phi}{\epsilon} + \frac{1}{\pi}\sin\left(\frac{\pi\phi}{\epsilon}\right)\right], & |\phi| < \epsilon \\ 1\,, & \phi > \epsilon \end{array} \right\} \qquad (5)$$

The solution of the distance function φ, if only solved for using Eq. 3, will deteriorate over time in areas of high velocity gradients or sharp turbulence. To remediate this, a re-distancing equation is employed in between timesteps, details of which are discussed in [70] .

2.2 Geometrical Setup

The experimental setup is designed to produce scaling information for a wire-to-cylinder plasma discharge, where the wire is a capillary (tube) that allows gas flow into the water, and the cylinder is a grounded electrode wrapped around a glass cylinder. The glass cylinder serves as dielectric barrier between driven (wire) and grounded (cylinder) electrode. As described in section 1.2, the wire-to-cylinder geometry is favorable for the distribution of electric field lines, which will be centered with high electric field strength around the driven electrode, i.e. the outlet of the gas flow. The capillary that serves as driven electrode has an inner diameter of 1 mm and is composed of stainless steel, with five equidistant orifices serving as openings for bubbles to form. Varying bubble shapes and sizes offer the possibility to adjust the required voltage for the plasma breakdown and will have an impact on the resulting chemistry in the bubble-liquid mixture. Further, it allows the fundamental investigation of plasma breakdown mechanisms in bubbles in liquids dependent on the bubble size and shape. Thus, a detailed understanding of the bubble formation and the impact of the capillary, the hole geometry, as well as the gas flow dynamics on the bubble formation is investigated in a simpler setup with flat glass panes forming a cuboid as that will allow for better optical analysis of the bubbles.

The setup for the simulations mirrors the previously described experimental setup, which is essentially a regular cuboidal tank with water filled up to 50 mm above the air inflow tube. The air inflow tube is a cylindrical metal pipe with five orifices drilled into it, each 0.5 mm in diameter and 10 mm apart (center-to-center). The tube itself has a 1 mm I.D. and an O.D. of 1.5875 mm (1/16 in.). Air flows horizontally into the tube and vertically upwards into the tank (see Fig. 3). Having a small vent rather than an open top tremendously saves on computation costs as we need to resolve a much smaller interface, allocating more computational elements in areas where fluid dynamics is critical, i.e. at and above each orifice. Thus, there is a small air vent (10x10x20 mm) at the top of the tank directly above the first two orifices in the pipe. The vent is off the center of the

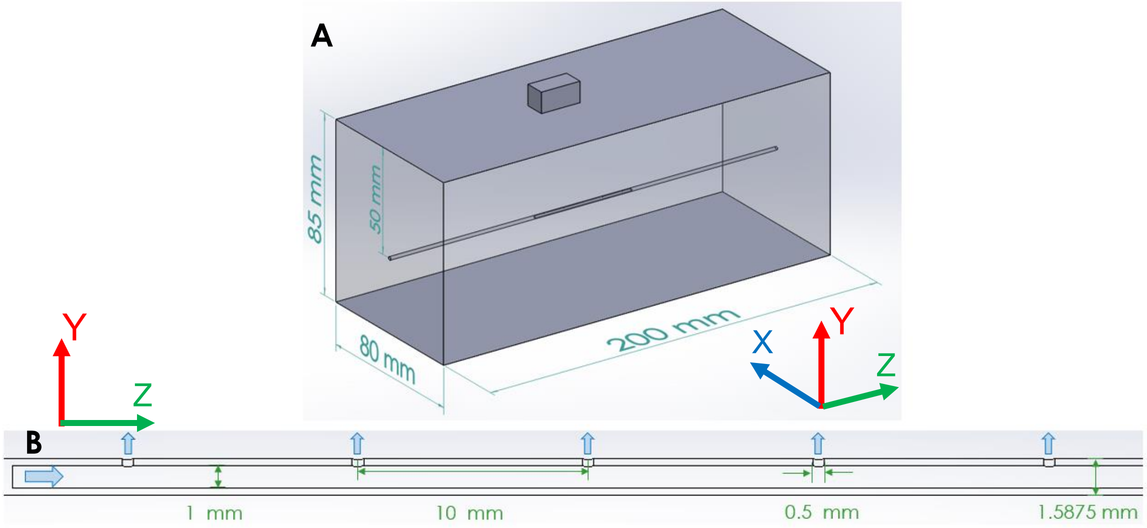

Fig. 3. *Computational domain:* ***A.*** *3-D model* ***B.*** *Zoom in on inner air tube*

domain (i.e. not directly above the third orifice) so as not to artificially interfere with phenomena at and around the orifices.

2.3 Computational Mesh Design

The computational domain (Fig. 3) was filled with unstructured mesh elements (tetrahedra) of various sizes depending on the proximity to the orifices (Fig. 4). The mesh was refined in cylindrical regions leading into each orifice, with much larger refinement regions present around orifices where bubble formation is expected (i.e. the first orifice for two-phase flow at 50 mL/min). Key features of this mesh are enumerated in Table 1.

2.3.1 Mesh Verification

While these mesh parameters were based on iterative testing to strike a balance between having enough resolution to capture bubble departure and being small enough to run at a reasonable pace on our local cluster, we have conducted a grid convergence study to show potential impact of further refinement or coarsening of the mesh on the

Table 1. Mesh parameters

Parameter		Value
Total number of mesh elements		4,197,675
Elements across orifice		18
Elements across inner pipe		12
Region 1[a]	Elements across diameter	22
	Element Size	166.7 µm
	Vertical Height (above nozzle)	24,000 µm
Region 2[a]	Elements across diameter	42
	Element Size	83.3 µm
	Vertical Height (above nozzle)	3,400 µm
Region 3[a]	Elements across diameter	42
	Element Size	41.7 µm
	Vertical Height (above nozzle)	150 µm

[a] See Fig. 4

bubble volume representation. These simulations were setup in a reduced version of the domain maintaining the water height (and thus, the hydrostatic pressure) and the dimensions of the pipe, but with only one orifice. Five cases were setup, wherein the size each of the elements in the focus area around the nozzle (i.e. the view seen in Fig. 4), were multiplied by a fraction of the base value (0.63, 0.79, 1.00, 1.26 and 1.59).

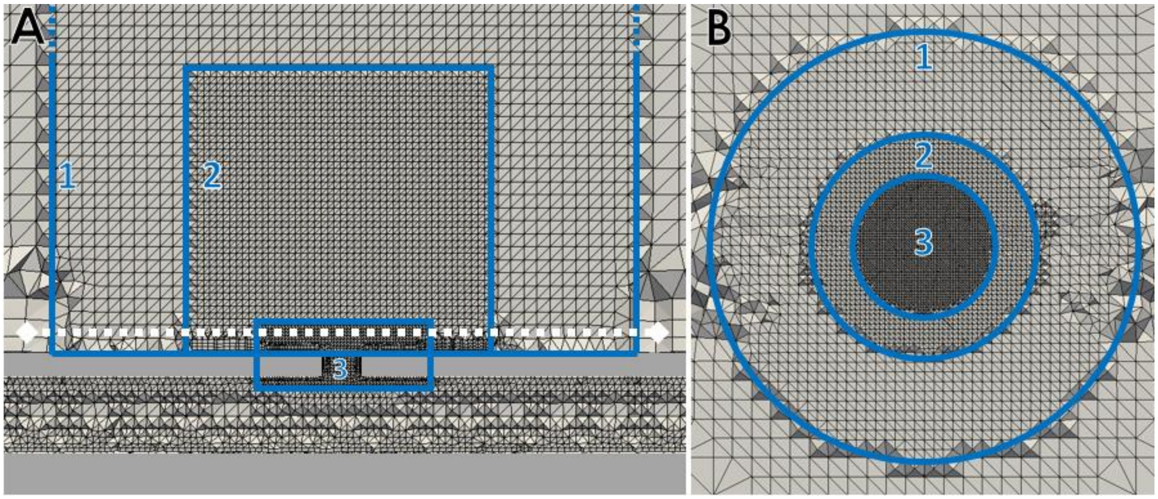

Fig. 4 *Slice of computational mesh showing three critical successive cylindrical refinement regions:* ***A.*** *Front View (vertical slice across the midplane of the pipe)* ***B.*** *Top View (horizontal slice 1 mm above the center of the pipe, shown by the white dotted line in* ***A****).*

These numbers were chosen so that the relative volume of the average tetrahedra formed would be 25%, 50%, 100%, 200% and 400%, respectively. Simulations were run with the same air inflow rate as the two-phase simulations in the results section (50 mL/min) until a few hundred time steps after the point of detachment of the first bubble, with results are presented in Table 2 and Table 3.

One aspect of what we looked at is how the mesh resolved the gas volume under both static and dynamic conditions (Table 2). The static condition was simply the initial condition and the volume of gas at the first timestep of each simulation was measured. The dynamic gas volume growth as determined by looking at how good the mesh was at mitigating the mass loss during the bubble injection process (a well-known issue in the level set method) [71]. To do so, we took the difference between the total gas volume 500 timesteps after breakup occurred and the total gas volume 500 timesteps after the initialization was completed (spanning several thousand timesteps depending on the mesh, or 30-45 ms of simulation time).

Table 2. Static and Dynamic Gas Volume Resolution based on Grid Volume

Relative Element Volume	Start Volume [mm^3]	Volume Added (Theory) [mm^3] [a]	Volume Added (Practice) [mm^3]	% Difference	Effective Flow Rate [mm^3/s]
400%	7.92	33.28	17.95	-46.1%	436.5
200%	7.96	37.89	27.00	-28.7%	578.5
100%	7.97	30.14	23.38	-22.4%	630.1
50%	7.98	27.82	21.96	-21.0%	644.7
25%	7.98	25.15	21.83	-13.2%	712.8

[a] Based on the inflow rate numerically measured near the inlet

Table 3. Effect of Mesh Resolution on Initial Bubble Formation

Relative Element Volume [a]	Bulk Element Edge Size [mm]	Relative Element Edge Size [a]	Detachment Time [ms]	First Bubble Volume [mm^3]	Number of Elements [b]
400%	8.46	1.59	54.20	24.23	653,933
200%	6.72	1.26	59.95	33.20	1,149,194
100%	5.33	1.00	50.36	31.58	1,937,951
50%	4.23	0.79	47.07	30.79	3,236,166
25%	3.36	0.63	43.73	30.67	5,751,417

[a] Relative to the main mesh used in this study (shown in Figure 4) in a truncated version of the domain described in Table 1.

[b] Due to the way the far-field elements were created (outside of the interest area), the number of elements does not scale exactly with relative element volume.

Due to the multi-tiered nature of the mesh (see Fig. 4) and the physics involved, simply looking at mass conservation is not enough. In addition, the bubble departure volume was examined as a parameter more heavily based on physics. A closer look at detachment times shows bubbles steadily departing earlier the finer the mesh (excepting that seen in the coarsest mesh). However, since the bubbles detach earlier the finer the mesh is, those bubbles end up being smaller. The most likely reason for this is that the finer mesh is able to resolve the undercurrent of water that pinches the bubble to cause detachment.

As we see in the results shown in Table 3, it is clear that the volume of the first bubble formed slowly converges to a value around 30.7 mm^3. In fact, the diameter of the bubble in the most-refined mesh (3.88 mm) is only about 10% greater than that predicted (3.51 mm) using the model developed by Gaddis & Vogelpohl based on a force balance at the orifice [72]. While close, this is certainly not an exact result. We attribute this minor difference to a combination of three factors: i) Gaddis & Vogelpohl based their theory on a nozzle shaped like that in Fig. 1B with negligible nozzle thickness, rather than that in our simulations (Fig. 1C) with considerable surface area for the interface to slide on; ii) Gaddis

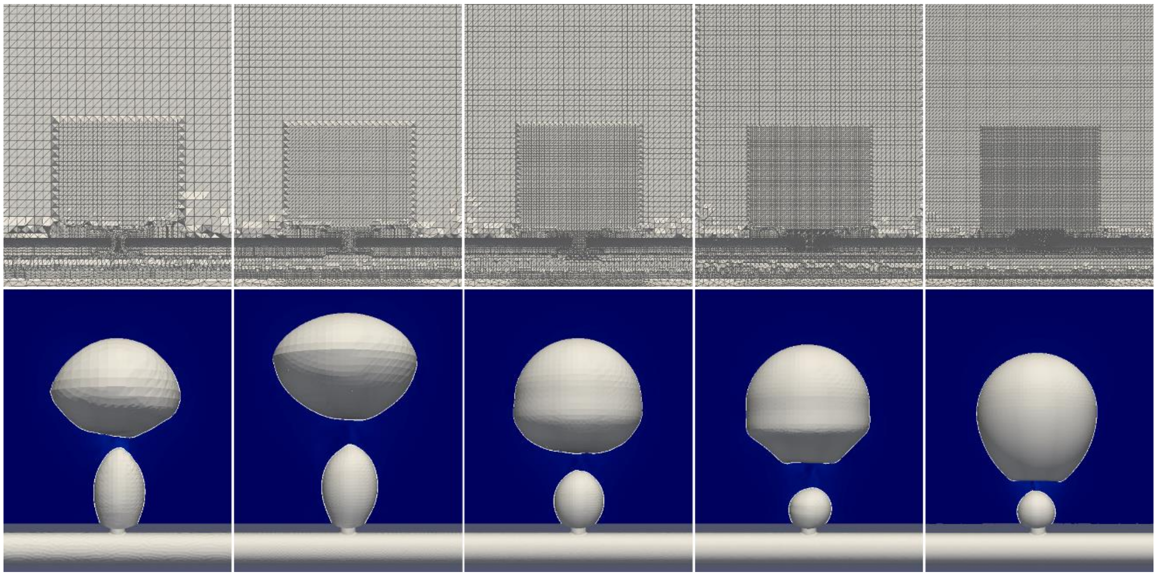

***Fig. 5** First bubbles to depart at various mesh sizes going from coarsest (left) to finest (right), with detailed parameters present in Table 3.*

& Vogelpohl assumed that there would be no residual gas at the nozzle after bubble detachment (i.e. that the nozzle would be nearly flush), which is not the case in our simulations (Fig. 5); iii) Gaddis & Vogelpohl assumed that spherical bubbles would form, but in our simulations we see non-spherical bubbles.

A mesh sensitivity study, including the computation of the grid convergence index (GCI) [73] has been performed using the middle three meshes from the above tests (Table 4) – one courser than that used in the main results section, and one finer. We note an order of convergence of 3.11, and monotonic asymptotic convergence with $\mathrm{GCI}_{\mathrm{fine}}^{12} =$ 5.79% and $\mathrm{GCI}_{\mathrm{fine}}^{23} =$ 2.98%.

Table 4. Mesh Sensitivity of Initial Bubble Volume

	Mesh 1		**Mesh 2**		**Mesh 3**
Total Number of Elements	1,149,194		1,937,951		3,236,166
First Bubble Volume [mm^3]	33.2		31.6		30.8
Relative Error $\lvert\varepsilon\rvert$		4.88%		2.50%	
$\mathrm{GCI}_{\mathrm{fine}}$		**5.79%**		**2.96%**	
Order of Convergence, p			3.11		

3 RESULTS & DISCUSSION

3.0 Validation

The experimental setup described in Section 2.2 was used to obtain quantitative results to provide validation for the simulations. As described in Section 1.2 and illustrated in Fig. 2, obtaining, and manipulating bubble shapes are critical to this study. Thus, experimental data collection also focused on capturing bubble profiles.

Images were taken using a DSLR camera (Canon EOS 6D) and evaluated using Matlab. The DSLR is placed at the lens's closest focusing distance (45 cm) away from and centered on the capillary. To capture bubble shape with as little blurring as possible the DSLR is set to the quickest shutter speed (1/4000 s) and largest aperture (f/4). To illuminate the bubbles an 800 lumen LED backlight (CREE LMH2) is positioned behind the apparatus with a diffuser. To process the images several frames of the experimental setup are captured without bubbles flowing. These images are used as a pseudo-flat-field image to correct for intensity reduction around the perimeter of the LED backlight. To ensure consistent framing of each image the DSLR is controlled remotely and triggered to shoot in continuous mode – capturing an image every 220 ms (4.5 fps). All images are loaded into Matlab where they are cropped, subtracted from the "flat-field-frames", converted to binary (black & white), and filled to capture the geometry (Fig. 6). Each bubble in each image can then be fitted to an ellipse to extrapolate major and minor axes, area (total number of pixels), axis-tilt, and position in the image. Area is calculated assuming an elliptical shape with the measured axes and compared to the observed area in pixels to

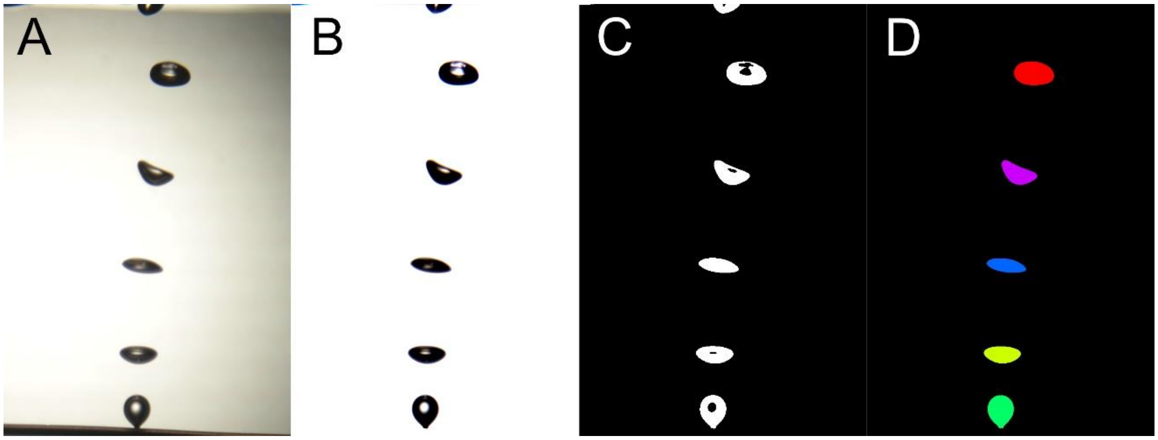

Fig. 6 *Processing of experimental bubble trains with an air inflow of 50 mL/min. (A) The original image is subtracted from a biasing image to (B) extract only the bubbles from the image . (C) The processed image is converted to binary and inverted. (D) The "holes" are filled in by MatLab and colored to identify the bubble.*

determine bubble deviation away from ellipticity. Likewise, volume must be extrapolated under the assumption of azimuthal symmetry and oblate ellipsoidal bubbles.

For time resolved data, an Apple iPhone XS camera is used to capture slow-motion video of the bubbles at the 240 fps capture setting. Due to the variable frame rate (VFR) of the video encoder used for this device the average, minimum, and maximum framerates must be determined from the metadata of each file. On average this device captures 240.19 ± 26.60 fps, or 4.1634 ± 0.4621 ms between frames\average framerate and error were calculated for each video. The lower image resolution of the video (720p) as compared to the DSLR results in a loss of spatial data. At the distance of image capture (45 cm), this results in a reduction in resolution from roughly 25 µm per pixel (Canon EOS 6D) to 110 µm per pixel (iPhone XS). Each frame of the video can be exported as an image file and run through Matlab in the same manner as the still images. To calculate differential volume of bubble formation the Matlab output data for each frame can extract the bubble at the nozzle position (minimum y-position) and used to plot the calculated volume at each time-step between frames. As such, the slow-motion feature must be used when capturing time-resolved behavior at flows greater than 5 mL/min, otherwise, the spatial resolution captured through the DSLR is used to determine cross-sectional area, ellipticity deviation, position, and calculated volume (Table 5). From the spatially resolved data the major/minor diameters and eccentricity of the fitted ellipse of each bubble can be plotted as a function of distance from the nozzle (Fig. 7, Fig. 8). The eccentricity is a parameter of an ellipse that characterizes its shape,

$$e = \sqrt{1 - {b^2}/{a^2}} \tag{6}$$

where *a* is the major-axis radius, and *b* is the minor-axis radius. A circle has an eccentricity of *e* = 0 and a straight line (*b* = 0) has an eccentricity of *e* = 1. The shape of the bubbles from experiment show a consistent evolution and size from formation to detachment and as they traverse to the surface. During formation, bubble size increases linearly with *a≈b*, while after detachment major (*a*) and minor (*b*) radii diverge and eccentricity reaches a constant value around *e* = 0.9.

Table 5. Spatial Data Generated by Bubble Imaging

position[a] [mm]	**a[b] [mm]**	**b[c] [mm]**	**A_{meas}[d] [mm^2]**	**A_{calc}[e] [mm^2]**	**V_{calc}[f] [mm^3]**	**Ellipse Deviation [% difference]**
(4.896 , 2.874)	1.544	1.281	6.113	6.212	12.788	1.601
(4.765 , 7.817)	1.923	1.064	6.331	6.428	16.477	1.513
(4.555 , 17.05)	2.005	0.914	5.758	5.758	15.388	0.864
(4.199 , 27.69)	2.292	0.825	5.722	5.941	18.156	3.687
(1.797, 38.55)	2.148	1.091	7.307	7.358	21.068	0.685

[a] ((z,y) positions from the first orifice)
[b] (major axis of ellipse imposed over bubble)
[c] (minor axis of ellipse imposed over bubble)
[d] (area calculated by pixel count of filled section of bubble)
[e] (area calculated for axes, A=πab)
[f] (volume of bubble calculated assuming azimuthally symmetric oblate ellipsoid $V = (4/3)\, a \cdot A_{meas}$)

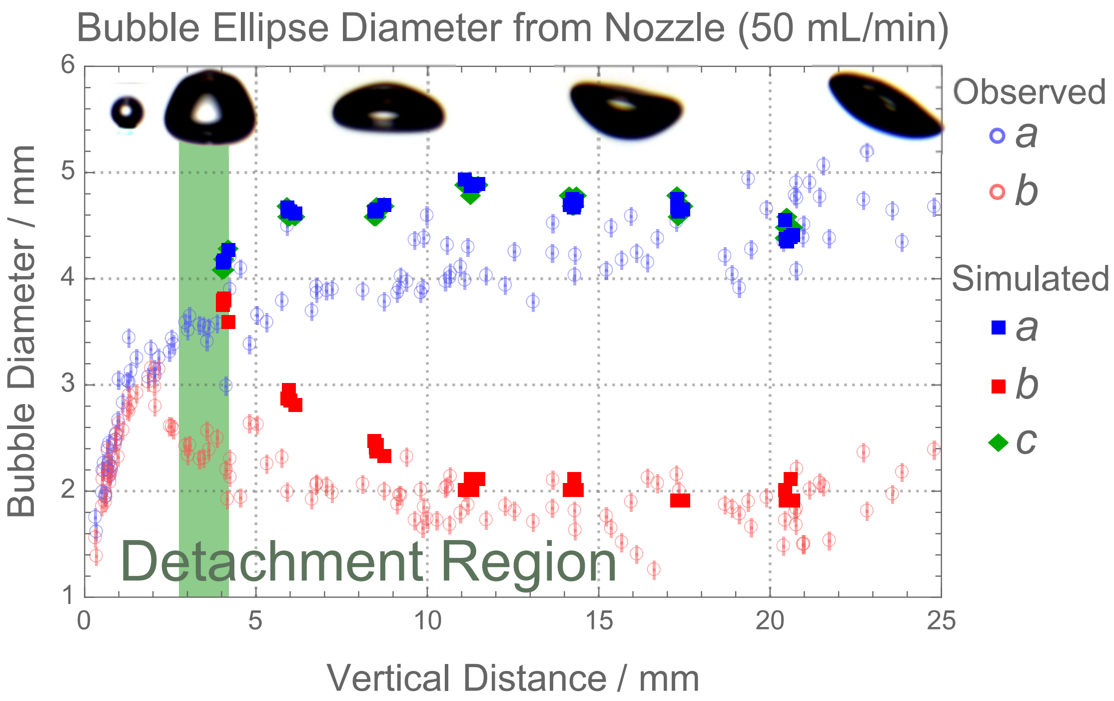

Fig. 7 *Plot of major and minor diameters of the fitted ellipse of individual bubbles as a function of distance from the nozzle. The detachment region is highlighted in green. Bubble images are superimposed at the distances at which they appear in a single frame.*

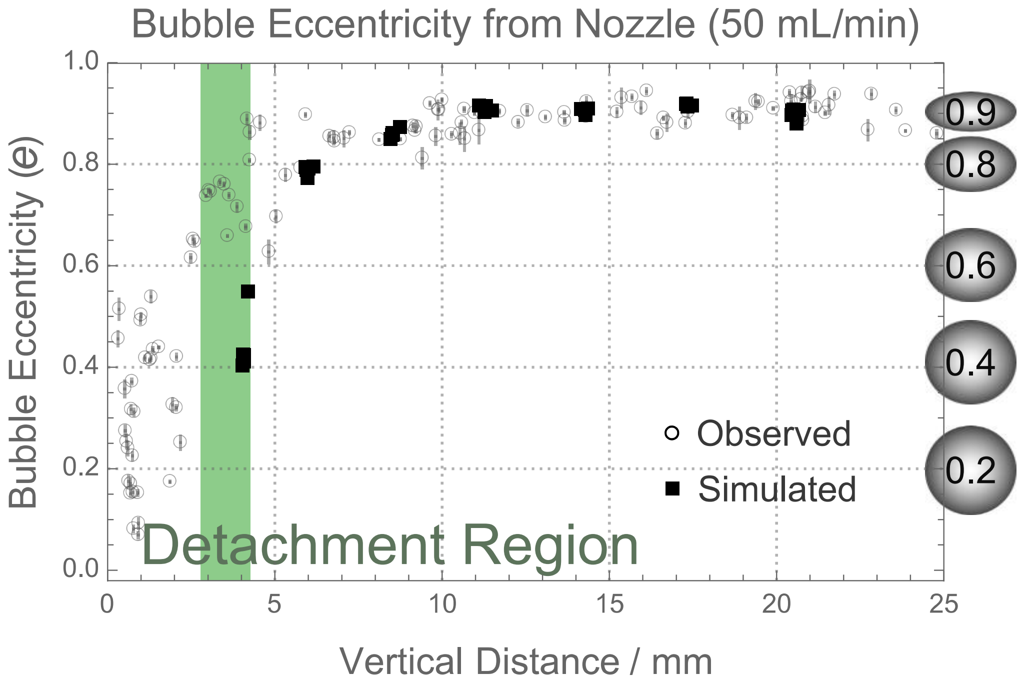

Fig. 8 *Plot of the eccentricity of a fitted bubble as a function of vertical distance from the nozzle. The detachment region is highlighted in green. The shape of an ellipse is illustrated next to the corresponding eccentricity.*

3.1 Single Phase Air Flow Through the Domain

In order to enhance our understanding of how this orifice configuration may affect the fluid dynamics of the system, we conducted a single phase simulation with air inflow at 200 mL/min, allowing the air to pass through the entire domain several times before capturing results. Before entering any orifices, the air velocity in the pipe formed a parabolic profile (Fig. 9, Fig 10a). However, the air directly following the first orifice was biased towards the top side of the tube (Fig. 10b). This can be explained by the localized pressure build-up at the bottom-right side of the first orifice (Fig. 11). This behavior is consistently noted at all five orifices (Fig. 10, Fig. 11), albeit to lesser extents as the flow escapes through the orifices. We can see the trend in flow attenuation across the orifices in Table 6 – where 50% of the flow ejects through the first two orifices and only 0.07% of the flow remains as recirculation past the fifth orifice.

Upon closer examination of Fig. 9, we can see that the jets produced from the orifices do not follow a trajectory that is fully perpendicular to the inflow axis. Instead, a slight deviation towards the inflow direction (i.e. the positive z axis) is observed. This deviation in jet flow is most pronounced in the first orifice, where the pressure buildup is also most pronounced (Fig. 11), and regresses slowly towards a vertical line as the flow escapes through the orifices and the pressure effect is less pronounced. This effect also comes into play in our two-phase simulations.

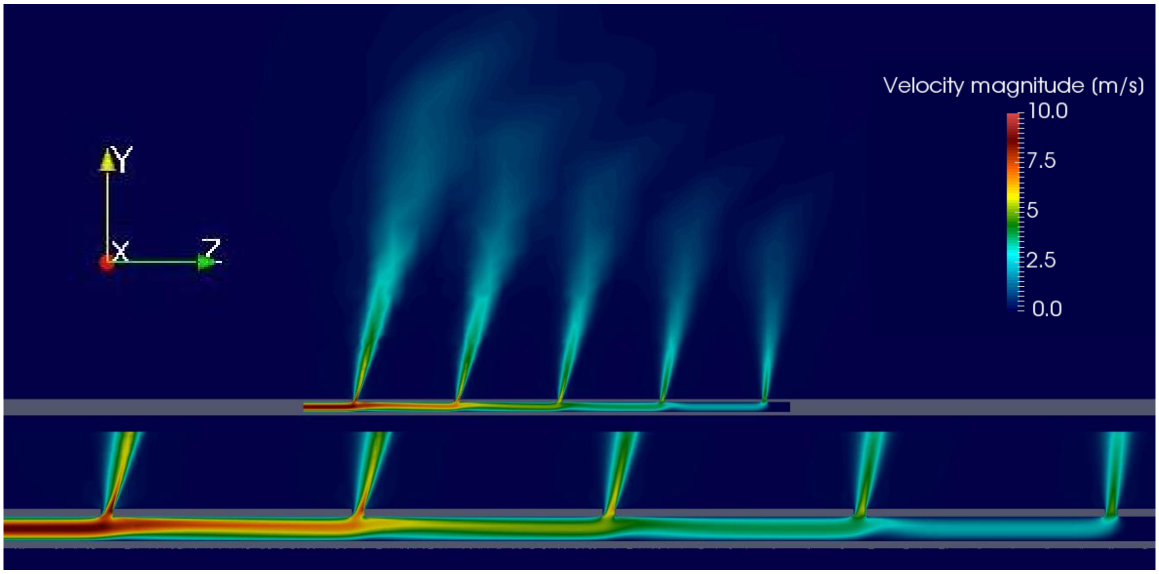

Fig. 9 Single phase flow distribution along the pipe.

Table 6. Single Phase Flow Distribution Within the Pipe

z^a [m]	<v> [m/s]	Re	Flow Rate [ml/min]	Flow Rate [% of inflow]
-0.025	4.14	269.75	200.00	100.00%
-0.015	2.99	195.04	144.61	72.31%
-0.005	2.03	132.31	98.10	49.05%
+0.005	1.23	80.36	59.58	29.79%
+0.015	0.57	37.48	27.79	13.90%
+0.025	0.00	0.19	0.14	0.07%

[a] (where z = -0.02 is the position of the first orifice, and z = +0.02 is the position of the fifth orifice)

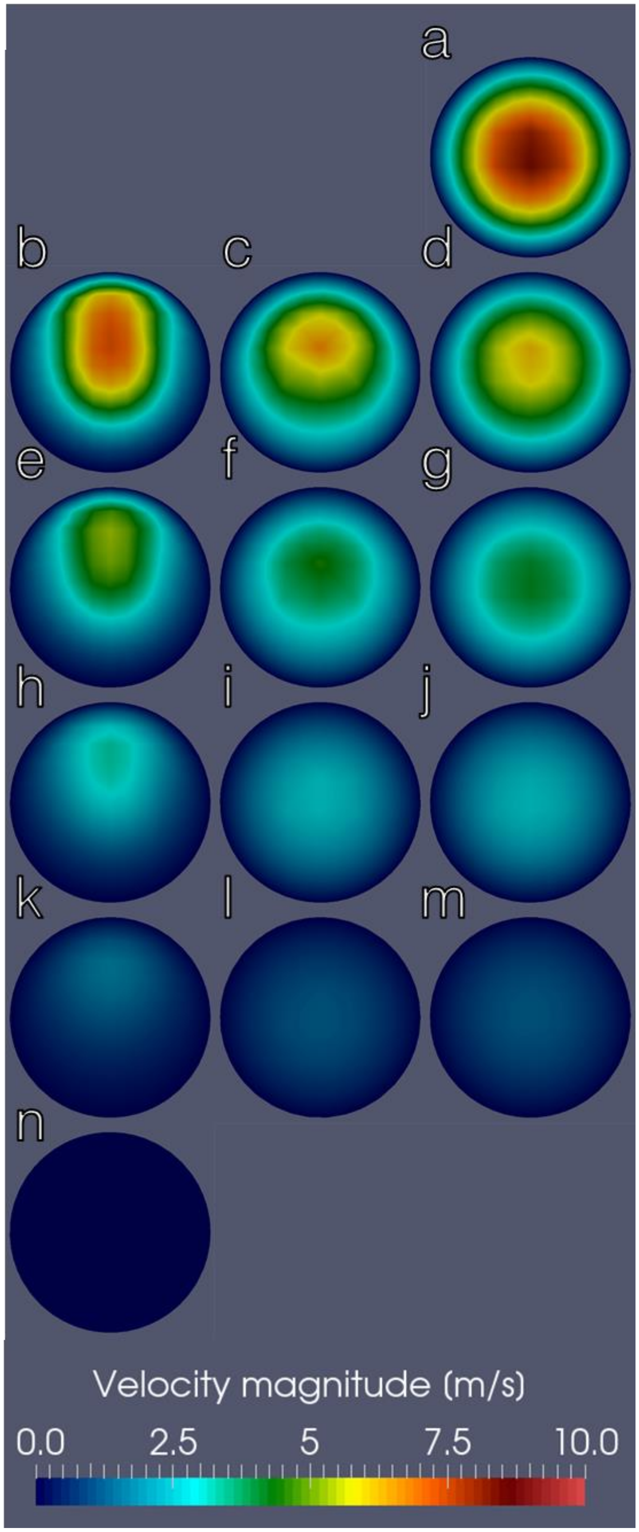

Fig. 10 *Single phase flow distribution at various cross-sections. From top to bottom, left to right, the cross section positions are: z = -0.021, -0.019, -0.015, -0.011, -0.009, -0.005, -0.001, +0.001, +0.005, +0.009, +0.011, +0.015, +0.019, +0.021.*

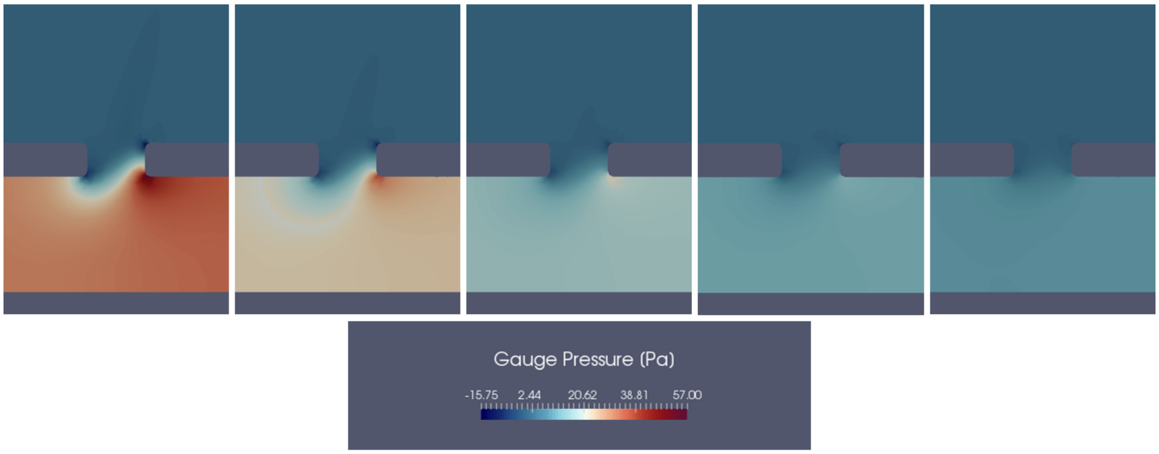

Fig. 11 *Gauge pressure at each orifice during single phase flow.*

3.2 Bubble Formation

The bubble formation process with air inflow of 50 mL/min was found to be remarkably consistent (Fig. 12), excepting the formation of the first two bubbles. This can be accounted for by noting that: i) the initialization process may have been sufficient to fully stabilize the first bubble to depart; ii) the first bubble to depart has no wake above it; iii) the second bubble to depart experiences the wake of the first departed bubble, which is unsteady because the first bubble has no wake above it. By the time the third bubble departs, the wake stream has stabilized enough such that repetitive behavior can be observed, which is seen quantitatively in Table 7. Close examination of the bubbles that trail departure events 1-8 (Fig. 13) shows successive leaning, like the phenomena observed in Fig. 9, but to a much lesser extent.

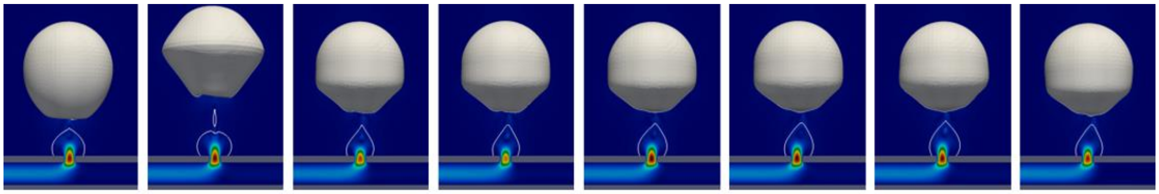
101.7 ms **157.6 ms** **205.4 ms** **254.5 ms** **303.1 ms** **351.9 ms** **400.4 ms** **448.1 ms**

Fig. 12 *Bubble Departure for eight successive bubbles at 50 mL/min*

Table 7. Bubble Formation Characteristics at 50 mL/min

	Bubble Number							
	1	2	3	4	5	6	7	8
Formation Time [ms]	101.7	55.9	47.8	49.1	48.6	48.8	48.5	47.7
Expected Volume[a] [mm^3]	84.8	46.6	39.8	40.9	40.5	40.7	40.4	39.8
Simulation Volume [mm^3]	36.3	36.3	33.4	33.6	33.3	33.6	33.2	33.3
Mass defect (%)	-57%	-22%	-16%	-18%	-18%	-17%	-18%	-16%

[a] Assuming that all of the air inflow contributes to the volume of the bubble at the first orifice

3.3 Bubble Evolution After Departure

3.3.1 Increase in eccentricity

As the bubbles form and rise, we see a clear trend in the bubble shape: an increase in the eccentricity of the bubbles. Since eccentricity is typically defined for a 2D ellipse, and the bubbles we see represent oblate spheroids (b>a, a≈c) (Fig. 7), we can use a modified form of Eq. 6 to represent the eccentricity of our bubbles,

$$e_{bub} = \sqrt{1 - \left(\frac{2b}{a+c}\right)^2} \tag{7}$$

where *a* is the major-axis radius, and *b* is the minor-axis radius, and c is the secondary major axis (perpendicular to *b*). Note at the radii *a*, *b*, and *c* are calculated along the co-ordinate axes x, y, and z respectively. In order to capture imperfections in the bubble

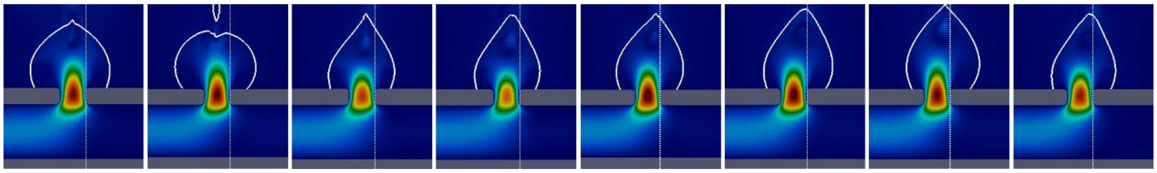

Fig. 13 *Progressive leaning of remnant bubbles after departure events 1-8 (from left to right). The dotted line is parallel to the outermost edge of the nozzle in this plane. Each subsequent bubble progressively leans further to the right so while the tip of bubble #1 is nearly above the center of the nozzle, the tip of bubble #8 is just over the outermost edge of the nozzle.*

shape with respect to the co-ordinate axes, we can use the following equation:

$$R_{imperfect} = \frac{V_{simulation}}{(\frac{4}{3} \cdot \pi \cdot abc)} \tag{8}$$

where a value of unity for $R_{imperfect}$ represents a perfect ellipsoid, whose axes are aligned along co-ordinate axes. As the bubbles rise, we see an overall decreasing trend in $R_{imperfect}$ (Fig. 14). The greatest decrease in this parameter is seen within after the first ten milliseconds of departure (after the bubbles have travelled on average 2 mm vertically), which is when the bubble are seeing the greatest increase in eccentricity, and are thus experiencing the most deformation.

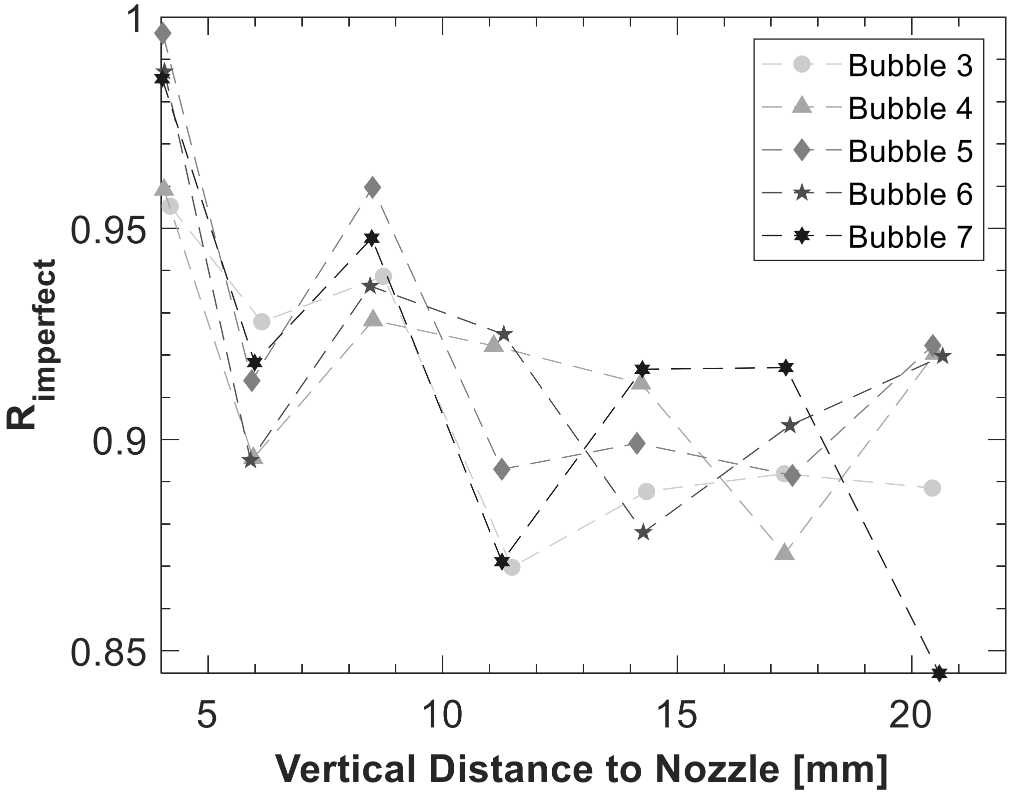

Fig. 14 *Plot showing the decrease in alignment along cartesian axes during bubble ascension. Data points for each bubble are extracted every 10 milliseconds of simulation time.*

We also note that as the local vertical velocity within the rising bubbles is not homogenous (Fig. 15); instead, oscillations can be observed between locally higher velocities on the edges with lower velocities in the midframe (frames 2,4, and 6 of Fig. 15), and higher velocities in the midframe (frames 1,3, and 5 of Fig. 15). When a bubble forms, the bulk velocity is in the bubble midframe, pushing it upward until it experiences increased resistance due to drag. At this point, the momentum of the bubble is diverted to the edges, which then rise above the bulk bubble mass subsequently causing them to experience more drag, and slow down, allowing the bulk mass to carry the bubble momentum once again.

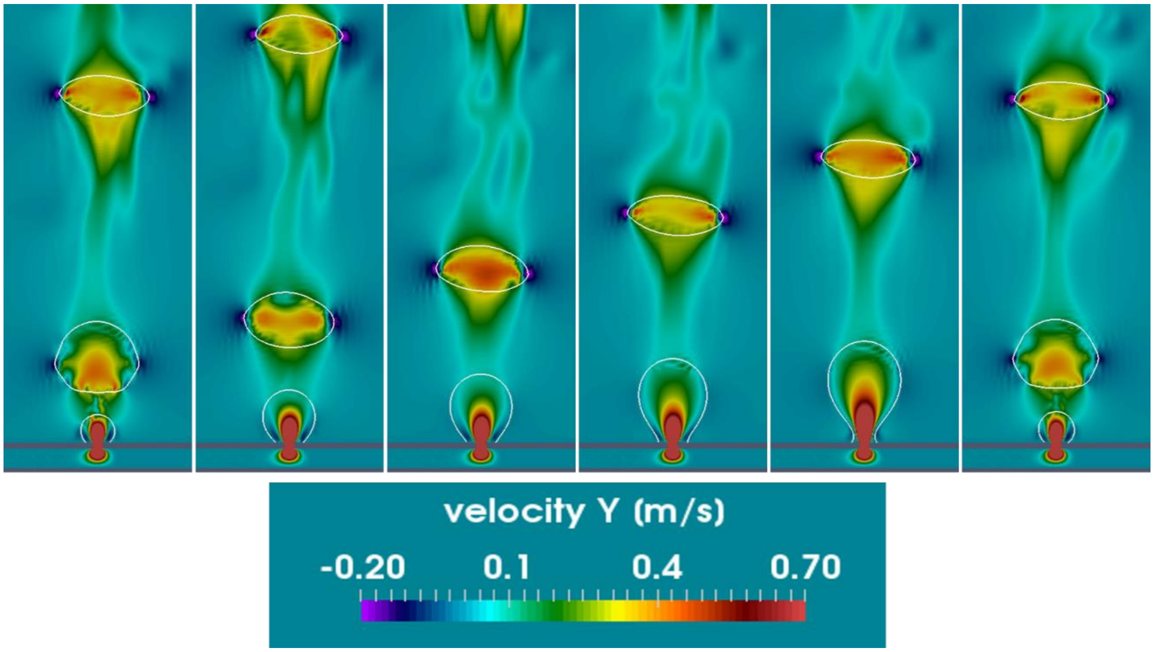

Fig. 15 *Successive snapshots of a rising bubble. The velocity scale has been selected to highlight the local velocity changes within and around the bubble, thus the velocity gradient at the nozzle is not visible. This figure tracks the position of bubble #3 for 60 ms, with 10 ms passing in between each frame. Bubble # 2 is visible in the first 2 frames, and the formation and departure of bubble #4 can also be seen.*

3.3.2 Bubble velocity components

The bulk of the bubble velocity is directed in the vertical direction (Fig. 16), with 1-5% of the bubble velocity in the tangential directions (Fig. 17). We note that while the bubbles do not quite reach terminal velocity, each successive bubble is slightly faster on average – this is likely due to the increased development of the wake region, allowing the bubble to flow upward more easily. While the variations in the X direction (normal to slice in Fig. 2B) appear stochastic, there is a noticeable trend in the Z velocities (Fig. 17). In particular, the Z velocities increase in the -Z direction (to the left looking at the plane in Fig. 2B or Fig. 15). This deviation did not occur as a direct result of the flow bias in the system (due to the inflow being in the +z direction, or to the right in Fig. 2B & Fig. 15), but rather, is likely to have occurred due to a stochastic result exacerbated by stabilization in the bubble wake. That is, when one bubble departs significantly in a certain direction, others are more likely to follow. This is clearly seen in Fig. 18, which shows the bubble positions relative to the nozzle in the X and Z directions. For the first 10 millimeters of rising, the bubbles follow a very consistent trajectory, likely where the wake is most well-established. Past that point, stochastic variations in bubble velocity are able to steer to bubble away from the “comfort” of any pre-established wake region.

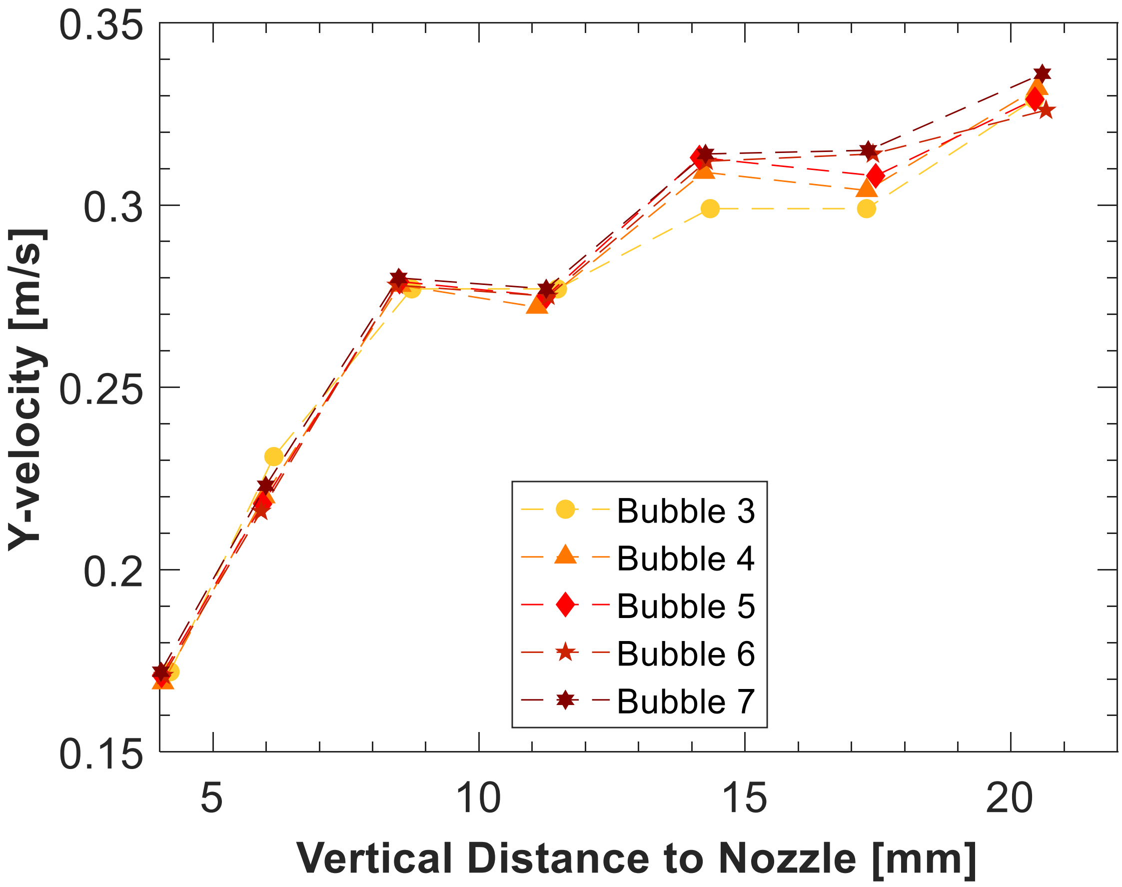

Fig. 16 *Increase in bubble rise velocity during bubble ascent*

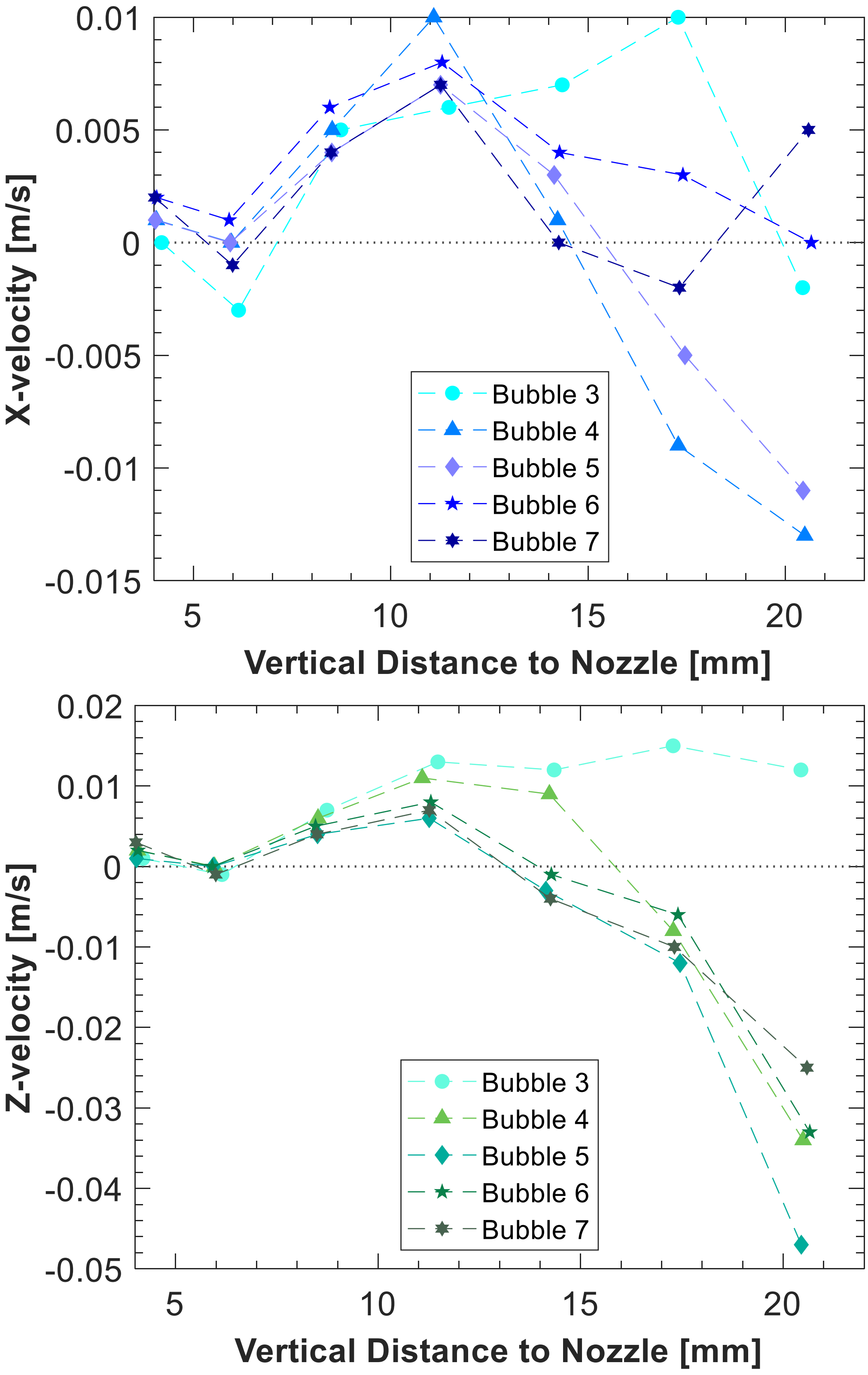

Fig. 17 *Variation in tangential components of bubble velocity (X - blue and Z - green) about the nozzle center.*

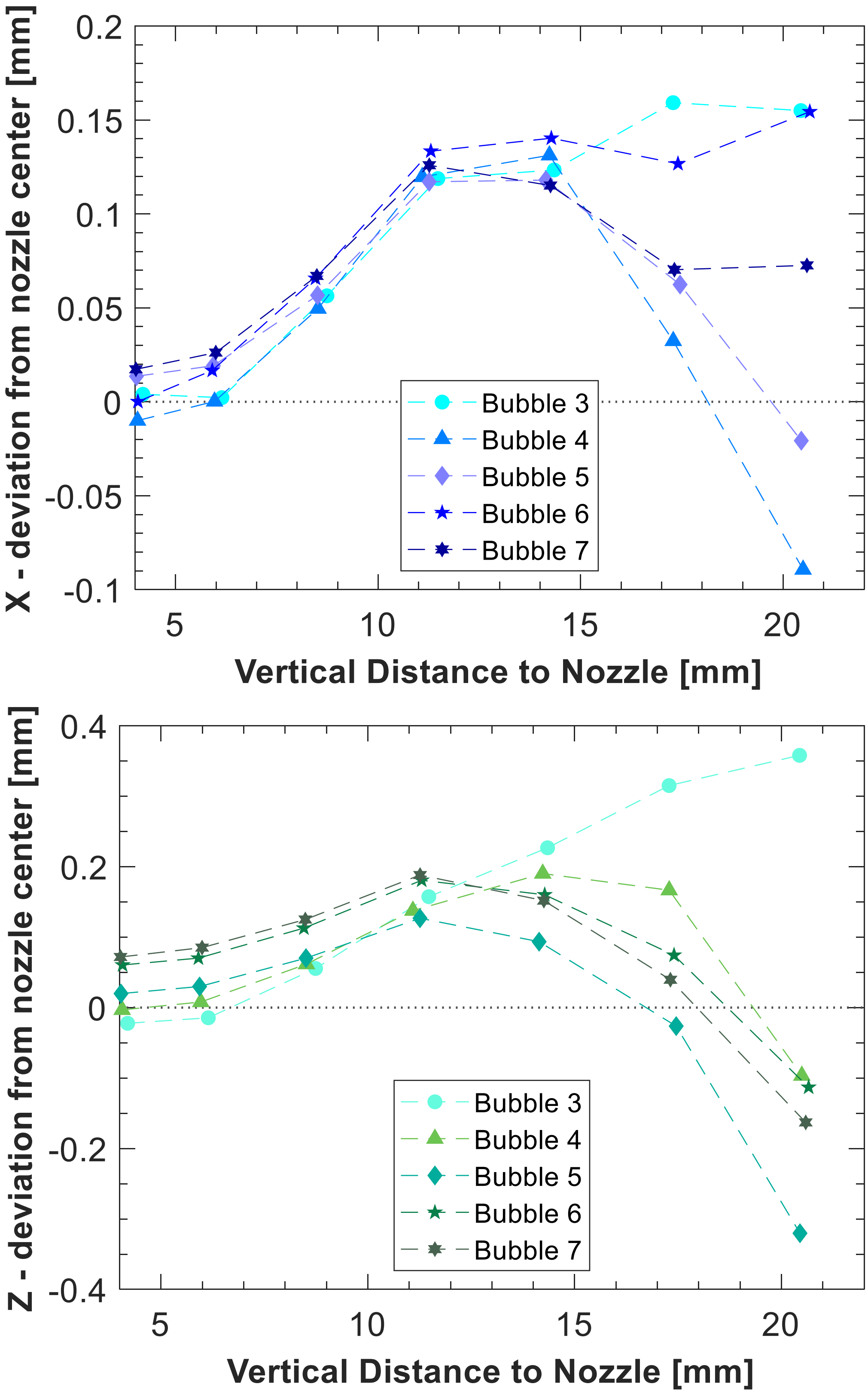

Fig. 18 *Tangential deviation in bubble center of mass about the nozzle center.*

4 CONCLUSIONS

In this study, we have investigated bubble formation in a novel variation of the conventional orifice problem: through a cylindrical pipe submerged in water with 0.5 mm holes drilled into it with air injected into through the side at 50 mL/min (Fig. 2B). At this flow rate, bubbles only came out of the first of five nozzles in both experiments and simulations. Bubble eccentricity sharply rose as soon as each bubble departed and approached an asymptote around e = 0.9. As the bubbles rose, imperfections also grew, causing the bubbles to deviate slightly away from a perfect ellipsoidal shape. Though the bubbles did not reach terminal velocity, there was a distinct flapping of the bubble edges throughout their ascent, due to periodic variations in the local velocities inside the bubble. Bubble wakes were seen to influence subsequent bubbles by i) allowing them to reach slightly higher vertical velocities and ii) stabilizing paths not necessarily perpendicular to the orifice.

ACKNOWLEDGMENTS

The authors acknowledge Altair Engineering, Inc. for their provision of the Acusim linear algebra solution library, and Simmetrix, Inc. for the libraries provided for mesh-building and domain modeling. We would also like to acknowledge the Argonne Leadership Computing Facility (ALCF) who have regularly provided us with supercomputer access that has allowed us to develop and enhance our parallel DNS code, PHASTA. Finally, we would like to acknowledge Dr. Mark Kushner for providing the code nonPDPSIM, used to generate the simulation seen in Fig. 2.

NOMENCLATURE

a	Major axis radius for an ellipse (or ellipsoid)
b	Minor axis radius for an ellipse (or ellipsoid)
c	Second major axis radius for an ellipsoid (prolate spheroid)
e	Eccentricity of an ellipse
e_{bub}	Equivalent eccentricity of an oblate spheroid
f	Body forces
H	Smoothed Heaviside function
P	Pressure field
$R_{imperfect}$	Ratio of bubble volume measured from a simulation to that calculated using assuming the bubble is an oblate spheroid aligned along coordinate axes
t	Time
u	Velocity vector
$V_{simulation}$	Bubble volume measured from a simulation
α	Generic fluid property variable
ε	Gas-Liquid interface thickness
μ	Dynamic viscosity
ϕ	Distance function for interface tracking
ρ	Density
τ	Viscous stress tensor

REFERENCES

[1] Zhang, L., and Shoji, M., 2001, "Aperiodic Bubble Formation from a Submerged Orifice," Chem. Eng. Sci., **56**(18), pp. 5371–5381.

[2] Qu, C., Yu, Y., and Zhang, J., 2017, "Experimental Study of Bubbling Regimes on Submerged Micro-Orifices," Int. J. Heat Mass Transf., **111**, pp. 17–28.

[3] Bai, H., and Thomas, B. G., 2001, "Bubble Formation during Horizontal Gas Injection into Downward-Flowing Liquid," Metall. Mater. Trans. B Process Metall. Mater. Process. Sci., **32**(6), pp. 1143–1159.

[4] Corchero, G., Montañés, J. L., and Corchero Téllez, J., 2012, "Effect of Flow Rate Conditions on Bubble Formation," Int. J. Heat Mass Transf., **55**(19–20), pp. 5044–5052.

[5] Lewis, D. A., and Davidson, J. F., 1983, "Bubble Sizes Produced by Shear and Turbulence in a Bubble Column," Chem. Eng. Sci., **38**(1), pp. 161–167.

[6] Balzan, M. A., Hernandez, F., Lange, C. F., and Fleck, B. A., 2019, "Parametric Study of the Frequency of Bubble Formation at a Single Orifice with Liquid Cross-Flow," J. Fluids Eng. Trans. ASME, **141**(9).

[7] Wen, J., Sun, Q., Sun, Z., and Gu, H., 2019, "Bubble Coalescence Efficiency near Multi-Orifice Plate," Chinese J. Chem. Eng., **27**(8), pp. 1765–1776.

[8] Xie, J., Zhu, X., Liao, Q., Wang, H., and Ding, Y. D., 2012, "Dynamics of Bubble Formation and Detachment from an Immersed Micro-Orifice on a Plate," Int. J. Heat Mass Transf., **55**(11–12), pp. 3205–3213.

[9] Valencia, A., Cordova, M., and Ortega, J., 2002, "Numerical Simulation of Gas Bubbles Formation at a Submerged Orifice in a Liquid," Int. Commun. Heat Mass Transf.

[10] Guillen, D. P., Cambareri, J., Abboud, A. W., and Bolotnov, I. A., 2018, "Numerical Comparison of Bubbling in a Waste Glass Melter," Ann. Nucl. Energy, **113**, pp. 380–392.

[11] Gerlach, D., Alleborn, N., Buwa, V., and Durst, F., 2007, "Numerical Simulation of Periodic Bubble Formation at a Submerged Orifice with Constant Gas Flow Rate," Chem. Eng. Sci., **62**(7), pp. 2109–2125.

[12] Simmons, J. A., Sprittles, J. E., and Shikhmurzaev, Y. D., 2015, "The Formation of a Bubble from a Submerged Orifice," Eur. J. Mech. B/Fluids, **53**, pp. 24–36.

[13] Fang, J., Cambareri, J. J., Li, M., Saini, N., and Bolotnov, I. A., 2020, "Interface-Resolved Simulations of Reactor Flows," Nucl. Technol., **206**(2), pp. 133–149.

[14] Puač, N., Gherardi, M., and Shiratani, M., 2018, "Plasma Agriculture: A Rapidly Emerging Field," Plasma Process. Polym., **15**(2), p. 1700174.

[15] Nzeribe, B. N., Crimi, M., Mededovic Thagard, S., and Holsen, T. M., 2019, "Physico-Chemical Processes for the Treatment of Per- And Polyfluoroalkyl Substances (PFAS): A Review," Crit. Rev. Environ. Sci. Technol., **49**(10), pp. 866–915.

[16] Banaschik, R., Lukes, P., Jablonowski, H., Hammer, M. U., Weltmann, K. D., and Kolb, J. F., 2015, "Potential of Pulsed Corona Discharges Generated in Water for the Degradation of Persistent Pharmaceutical Residues," Water Res., **84**, pp. 127–

135.

[17] Kolb, J. F., Joshi, R. P., Xiao, S., and Schoenbach, K. H., 2008, “Streamers in Water and Other Dielectric Liquids,” J. Phys. D. Appl. Phys.

[18] Bruggeman, P., and Leys, C., 2009, “Non-Thermal Plasmas in and in Contact with Liquids,” J. Phys. D. Appl. Phys.

[19] Stratton, G. R., Bellona, C. L., Dai, F., Holsen, T. M., and Thagard, S. M., 2015, “Plasma-Based Water Treatment: Conception and Application of a New General Principle for Reactor Design,” Chem. Eng. J., **273**, pp. 543–550.

[20] Babaeva, N. Y., Tereshonok, D. V., and Naidis, G. V., 2015, “Initiation of Breakdown in Bubbles Immersed in Liquids: Pre-Existed Charges versus Bubble Size,” J. Phys. D. Appl. Phys., **48**(35).

[21] Babaeva, N. Y., Naidis, G. V., Tereshonok, D. V., and Smirnov, B. M., 2017, “Streamer Breakdown in Elongated, Compressed and Tilted Bubbles Immersed in Water,” J. Phys. D. Appl. Phys.

[22] Kolobov, V. I., and Arslanbekov, R. R., 2011, “Towards Adaptive Kinetic-Fluid Simulations of Weakly Ionized Plasmas.”

[23] Tanaka, Y., 2009, “Thermally and Chemically Non-Equilibrium Modelling of Ar-N2-H2 Inductively Coupled Plasmas at Reduced Pressure,” Thin Solid Films, **518**(3), pp. 936–942.

[24] Kushner, M. J., 2009, “Hybrid Modelling of Low Temperature Plasmas for Fundamental Investigations and Equipment Design,” J. Phys. D. Appl. Phys., **42**(19), p. 194013.

[25] Shigeta, M., 2013, “Three-Dimensional Flow Dynamics of an Argon RF Plasma with Dc Jet Assistance: A Numerical Study,” J. Phys. D. Appl. Phys., **46**(1), p. 015401.

[26] Trelles, J. P., Chazelas, C., Vardelle, A., and Heberlein, J. V. R., 2009, “Arc Plasma Torch Modeling,” J. Therm. Spray Technol., **18**(5–6), pp. 728–752.

[27] Zhou, Q., Li, H., Xu, X., Liu, F., Guo, S., Chang, X., Guo, W., and Xu, P., 2009, “Comparative Study of Turbulence Models on Highly Constricted Plasma Cutting Arc,” J. Phys. D. Appl. Phys., **42**(1), p. 015210.

[28] Trelles, J. P., 2018, “Advances and Challenges in Computational Fluid Dynamics of Atmospheric Pressure Plasmas,” Plasma Sources Sci. Technol., **27**(9), p. 093001.

[29] Shigeta, M., 2016, “Turbulence Modelling of Thermal Plasma Flows,” J. Phys. D. Appl. Phys., **49**(49), p. 493001.

[30] Murphy, A. B., Tanaka, M., Yamamoto, K., Tashiro, S., Sato, T., and Lowke, J. J., 2009, “Modelling of Thermal Plasmas for Arc Welding: The Role of the Shielding Gas Properties and of Metal Vapour,” J. Phys. D. Appl. Phys., **42**(19), p. 194006.

[31] Norberg, S. A., Johnsen, E., and Kushner, M. J., 2015, “Formation of Reactive Oxygen and Nitrogen Species by Repetitive Negatively Pulsed Helium Atmospheric Pressure Plasma Jets Propagating into Humid Air,” Plasma Sources Sci. Technol., **24**(3).

[32] Lindsay, A. D., Graves, D. B., and Shannon, S. C., 2016, “Fully Coupled Simulation of the Plasma Liquid Interface and Interfacial Coefficient Effects,” J. Phys. D. Appl. Phys., **49**(23).

[33] Tian, W., and Kushner, M. J., 2014, “Atmospheric Pressure Dielectric Barrier

Discharges Interacting with Liquid Covered Tissue," J. Phys. D. Appl. Phys., **47**(16), p. 165201.

[34] Norberg, S. A., Tian, W., Johnsen, E., and Kushner, M. J., 2014, "Atmospheric Pressure Plasma Jets Interacting with Liquid Covered Tissue: Touching and Not-Touching the Liquid," J. Phys. D. Appl. Phys., **47**(47), p. 475203.

[35] Norberg, S. A., Parsey, G. M., Lietz, A. M., Johnsen, E., and Kushner, M. J., 2019, "Atmospheric Pressure Plasma Jets onto a Reactive Water Layer over Tissue: Pulse Repetition Rate as a Control Mechanism," J. Phys. D. Appl. Phys., **52**(1), p. 14.

[36] Tian, W., and Kushner, M. J., 2015, "Long-Term Effects of Multiply Pulsed Dielectric Barrier Discharges in Air on Thin Water Layers over Tissue: Stationary and Random Streamers," J. Phys. D. Appl. Phys., **48**(49), p. 494002.

[37] Kruszelnicki, J., Lietz, A. M., and Kushner, M. J., 2019, "Atmospheric Pressure Plasma Activation of Water Droplets," J. Phys. D. Appl. Phys., **52**(35), p. 355207.

[38] Babaeva, N. Y., and Kushner, M. J., 2008, "Streamer Branching: The Role of Inhomogeneities and Bubbles," IEEE Trans. Plasma Sci., **36**(4 PART 1), pp. 892–893.

[39] Babaeva, N. Y., and Kushner, M. J., 2009, "Structure of Positive Streamers inside Gaseous Bubbles Immersed in Liquids," J. Phys. D. Appl. Phys., **42**(13).

[40] Babaeva, N. Y., Tereshonok, D. V., Naidis, G. V., and Smirnov, B. M., 2015, "Initiation of Breakdown in Strings of Bubbles Immersed in Transformer Oil and Water: String Orientation and Proximity of Bubbles," J. Phys. D. Appl. Phys., **49**(2), p. 025202.

[41] Mededovic Thagard, S., Stratton, G. R., Dai, F., Bellona, C. L., Holsen, T. M., Bohl, D. G., Paek, E., and Dickenson, E. R. V., 2017, "Plasma-Based Water Treatment: Development of a General Mechanistic Model to Estimate the Treatability of Different Types of Contaminants," J. Phys. D. Appl. Phys., **50**(1), p. 014003.

[42] Banaschik, R., Jablonowski, H., Bednarski, P. J., and Kolb, J. F., 2018, "Degradation and Intermediates of Diclofenac as Instructive Example for Decomposition of Recalcitrant Pharmaceuticals by Hydroxyl Radicals Generated with Pulsed Corona Plasma in Water," J. Hazard. Mater., **342**, pp. 651–660.

[43] Banaschik, R., Burchhardt, G., Zocher, K., Hammerschmidt, S., Kolb, J. F., and Weltmann, K. D., 2016, "Comparison of Pulsed Corona Plasma and Pulsed Electric Fields for the Decontamination of Water Containing Legionella Pneumophila as Model Organism," Bioelectrochemistry, **112**, pp. 83–90.

[44] Ranieri, P., Sponsel, N., Kizer, J., Rojas-Pierce, M., Hernández, R., Gatiboni, L., Grunden, A., and Stapelmann, K., 2020, "Plasma Agriculture: Review from the Perspective of the Plant and Its Ecosystem," Plasma Process. Polym.

[45] Ingels, R., and Graves, D. B., 2015, *Improving the Efficiency of Organic Fertilizer and Nitrogen Use via Air Plasma and Distributed Renewable Energy*.

[46] Park, D. P., Davis, K., Gilani, S., Alonzo, C. A., Dobrynin, D., Friedman, G., Fridman, A., Rabinovich, A., and Fridman, G., 2013, "Reactive Nitrogen Species Produced in Water by Non-Equilibrium Plasma Increase Plant Growth Rate and Nutritional Yield," Curr. Appl. Phys., **13**(SUPPL.1), pp. S19–S29.

[47] Gierczik, K., Vukušić, T., Kovács, L., Székely, A., Szalai, G., Milošević, S., Kocsy, G., Kutasi, K., and Galiba, G., 2020, “Plasma-activated Water to Improve the Stress Tolerance of Barley,” Plasma Process. Polym., **17**(3), p. 1900123.

[48] Bradu, C., Kutasi, K., Magureanu, M., Puač, N., and Živković, S., 2020, “Reactive Nitrogen Species in Plasma-Activated Water: Generation, Chemistry and Application in Agriculture,” J. Phys. D. Appl. Phys., **53**(22), p. 223001.

[49] Chauvin, J., Judée, F., Yousfi, M., Vicendo, P., and Merbahi, N., “Analysis of Reactive Oxygen and Nitrogen Species Generated in Three Liquid Media by Low Temperature Helium Plasma Jet,” Sci. Rep.

[50] Šimečková, J., Krčma, F., Klofáč, D., Dostál, L., and Kozáková, Z., 2020, “Influence of Plasma-Activated Water on Physical and Physical-Chemical Soil Properties,” Water (Switzerland), **12**(9).

[51] Kurake, N., Ishikawa, K., Tanaka, H., Hashizume, H., Nakamura, K., Kajiyama, H., Toyokuni, S., Kikkawa, F., Mizuno, M., and Hori, M., 2019, “Non-Thermal Plasma-Activated Medium Modified Metabolomic Profiles in the Glycolysis of U251SP Glioblastoma,” Arch. Biochem. Biophys., **662**, pp. 83–92.

[52] Yan, D., Talbot, A., Nourmohammadi, N., Cheng, X., Canady, J., Sherman, J., and Keidar, M., 2015, “Principles of Using Cold Atmospheric Plasma Stimulated Media for Cancer Treatment OPEN.”

[53] Privat-Maldonado, A., and Bogaerts, A., 2020, “Plasma in Cancer Treatment,” Cancers (Basel)., **12**(9), pp. 1–3.

[54] Von Woedtke, T., Emmert, S., Metelmann, H. R., Rupf, S., and Weltmann, K. D., 2020, “Perspectives on Cold Atmospheric Plasma (CAP) Applications in Medicine,” Phys. Plasmas, **27**(7), p. 70601.

[55] Freund, E., Liedtke, K. R., Van Der Linde, J., Metelmann, H.-R., Heidecke, C.-D., Partecke, L.-I., and Bekeschus, S., “Physical Plasma-Treated Saline Promotes an Immunogenic Phenotype in CT26 Colon Cancer Cells in Vitro and in Vivo OPEN,” Sci. Rep.

[56] Tachibana, K., Takekata, Y., Mizumoto, Y., Motomura, H., and Jinno, M., 2011, “Analysis of a Pulsed Discharge within Single Bubbles in Water under Synchronized Conditions,” Plasma Sources Sci. Technol., **20**(3), p. 034005.

[57] Vanraes, P., Nikiforov, A., and Leys, C., 2012, “Electrical and Spectroscopic Characterization of Underwater Plasma Discharge inside Rising Gas Bubbles,” J. Phys. D. Appl. Phys., **45**(24), p. 245206.

[58] Kurahashi, M., Katsura, S., and Mizuno, A., 1997, “Radical Formation Due to Discharge inside Bubble in Liquid,” J. Electrostat., **42**(1–2), pp. 93–105.

[59] Zimmer, M. D., and Bolotnov, I. A., 2019, “Slug-to-Churn Vertical Two-Phase Flow Regime Transition Study Using an Interface Tracking Approach,” Int. J. Multiph. Flow, **115**, pp. 196–206.

[60] Zimmer, M. D., and Bolotnov, I. A., 2020, “Exploring Two-Phase Flow Regime Transition Mechanisms Using High-Resolution Virtual Experiments,” Nucl. Sci. Eng.

[61] Fang, J., Rasquin, M., and Bolotnov, I. A., 2017, “Interface Tracking Simulations of Bubbly Flows in PWR Relevant Geometries,” Nucl. Eng. Des., **312**, pp. 205–213.

[62] Fang, J., Cambareri, J. J., Rasquin, M., Gouws, A., Balakrishnan, R., Jansen, K. E., and Bolotnov, I. A., 2019, “Interface Tracking Investigation of Geometric Effects on the Bubbly Flow in PWR Subchannels,” Nucl. Sci. Eng., **193**(1–2), pp. 46–62.

[63] Bolotnov, I. A., 2013, “Influence of Bubbles on the Turbulence Anisotropy,” J. Fluids Eng. Trans. ASME, **135**(5).

[64] Brackbill, J. U., Kothe, D. B., and Zemach, C., 1992, “A Continuum Method for Modeling Surface Tension,” J. Comput. Phys., **100**(2), pp. 335–354.

[65] Nagrath, S., Jansen, K. E., and Lahey, R. T., 2005, “Computation of Incompressible Bubble Dynamics with a Stabilized Finite Element Level Set Method,” Comput. Methods Appl. Mech. Engrg, **194**, pp. 4565–4587.

[66] Jansen, K. E., 1999, *Computer Methods in Applied Mechanics and Engineering A Stabilized Finite Element Method for Computing Turbulence*.

[67] Whiting, C. H., and Jansen, K. E., 2001, “A Stabilized Finite Element Method for the Incompressible Navier-Stokes Equations Using a Hierarchical Basis,” Int. J. Numer. Methods Fluids, **35**(1), pp. 93–116.

[68] Sussman, M., Almgren, A. S., Bell, J. B., Colella, P., Howell, L. H., and Welcome, M. L., 1999, *An Adaptive Level Set Approach forIncompressible Two-Phase Flows*.

[69] Sethian., J. A., 1999, *Level Set Methods and Fast Marching Methods : Evolving Interfaces in Computational Geometry, Fluid Mechanics, Computer Vision, and Materials Science*, Cambridge, U.K. ; New York : Cambridge University Press, 1999.

[70] Sussman, M., and Fatemi, E., 1999, “Efficient, Interface-Preserving Level Set Redistancing Algorithm and Its Application to Interfacial Incompressible Fluid Flow,” SIAM J. Sci. Comput., **20**(4), pp. 1165–1191.

[71] Ménard, T., Tanguy, S., and Berlemont, A., 2007, “Coupling Level Set/VOF/Ghost Fluid Methods: Validation and Application to 3D Simulation of the Primary Break-up of a Liquid Jet,” Int. J. Multiph. Flow, **33**(5), pp. 510–524.

[72] Gaddis, E. S., and Vogelpohl, A., 1986, “Bubble Formation in Quiescent Liquids under Constant Flow Conditions,” Chem. Eng. Sci., **41**(1), pp. 97–105.

[73] Celik, I. B., Ghia, U., Roache, P. J., Freitas, C. J., Coleman, H., and Raad, P. E., 2008, “Procedure for Estimation and Reporting of Uncertainty Due to Discretization in CFD Applications,” J. Fluids Eng. Trans. ASME, **130**(7), pp. 0780011–0780014.

Figure Caption List

Fig. 1	Various orifice configurations: **A.** Conventional plate orifice **B.** Thin pipe as seen in [2] **C.** Our configuration with air cross-flow.
Fig. 2	Electric field concentration in bubbles due to permittivity differences and proximity effects of adjacent bubbles.
Fig. 3	Computational domain: **A.** 3-D model **B.** Zoom in on inner air tube.
Fig. 4	Slice of computational mesh showing three critical successive cylindrical refinement regions: A. Front View (vertical slice across the midplane of the pipe) B. Top View (horizontal slice 1 mm above the center of the pipe, shown by the white dotted line in A).
Fig. 5	First bubbles to depart at various mesh sizes going from coarsest (left) to finest (right), with detailed parameters present in Table 3.
Fig. 6	Processing of experimental bubble trains with an air inflow of 50 mL/min. (A) The original image is subtracted from a biasing image to (B) extract only the bubbles from the image . (C) The processed image is converted to binary and inverted. (D) The “holes” are filled in by MatLab and colored to identify the bubble.
Fig. 7	Experimental Images: **A.** Raw image **B.** Processed image after dividing out “flat-field images” **C.** Image after thresholding to binary and pixel inversion **D.** Image after “fill hole” command and coloring individual fill regions.
Fig. 8	Plot of the eccentricity of a fitted bubble as a function of vertical distance from the nozzle. The detachment region is highlighted in green. The shape of an ellipse is illustrated next to the corresponding eccentricity.
Fig. 9	Single phase flow distribution along the pipe
Fig. 10	Single phase flow distribution at various cross-sections. From top to bottom, left to right, the cross section positions are: z = -0.021, -0.019, -0.015, -0.011, -0.009, -0.005, -0.001, +0.001, +0.005, +0.009, +0.011, +0.015, +0.019, +0.021.
Fig. 11	Gauge pressure at each orifice during single phase flow
Fig. 12	Bubble Departure for eight successive bubbles at 50 mL/min
Fig. 13	Progressive leaning of remnant bubbles after departure events 1-8. The dotted line is parallel to the outermost edge of the nozzle in this plane. Each subsequent bubble progressively leans further to the right so while

	the tip of bubble #1 is nearly above the center of the nozzle, the tip of bubble #8 is just over the outermost edge of the nozzle.
Fig. 14	Plot showing the decrease in alignment along cartesian axes during bubble ascension. Data points for each bubble are extracted every 10 milliseconds of simulation time.
Fig. 15	Successive snapshots of a rising bubble. The velocity scale has been selected to highlight the local velocity changes within and around the bubble, thus the velocity gradient at the nozzle is not visible. This figure tracks the position of bubble #3 for 60 ms, with 10 ms passing in between each frame. Bubble # 2 is visible in the first 2 frames, and the formation and departure of bubble #4 can also be seen.
Fig. 16	Increase in bubble rise velocity during bubble ascent
Fig. 17	Variation in tangential components of bubble velocity (X - blue and Z - green) about the nozzle center
Fig. 18	Tangential deviation in bubble center of mass about the nozzle center

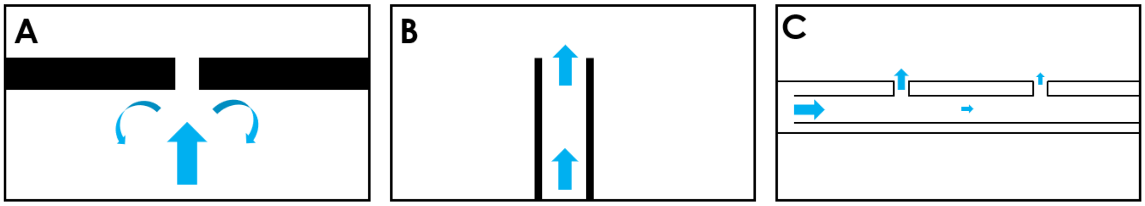

Fig. 1 Various orifice configurations: **A.** Conventional plate orifice **B.** Thin pipe as seen in [2] **C.** Our configuration with air cross-flow

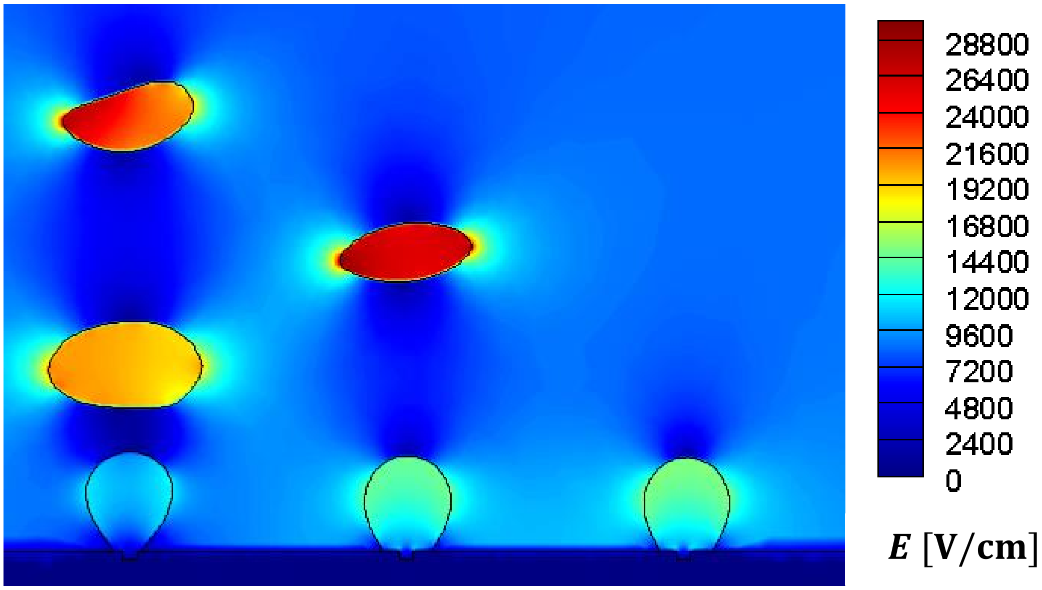

Fig. 2 Electric field concentration in bubbles due to permittivity differences and proximity effects of adjacent bubbles

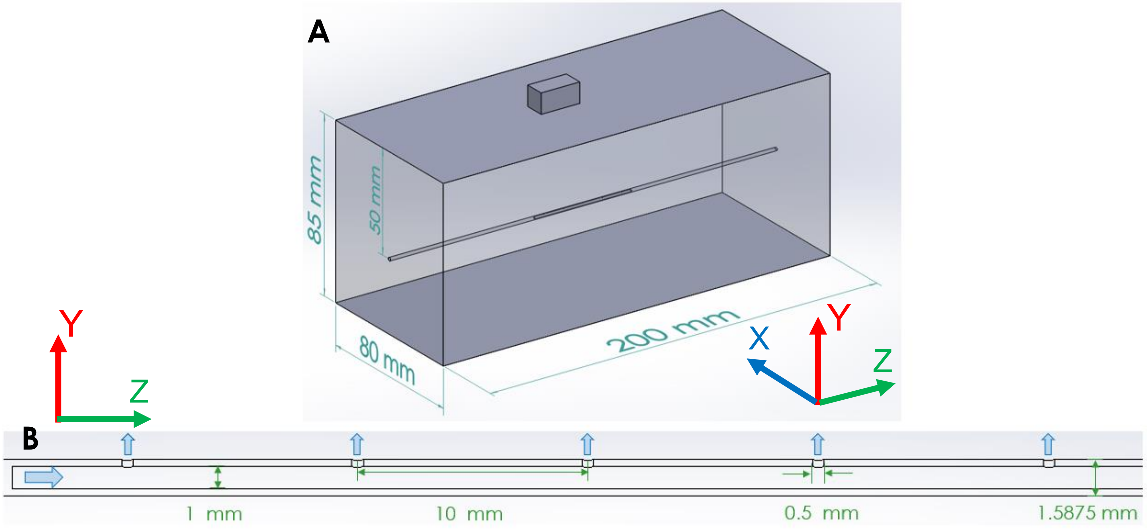

Fig. 3 Computational domain: **A.** 3-D model **B.** Zoom in on inner air tube

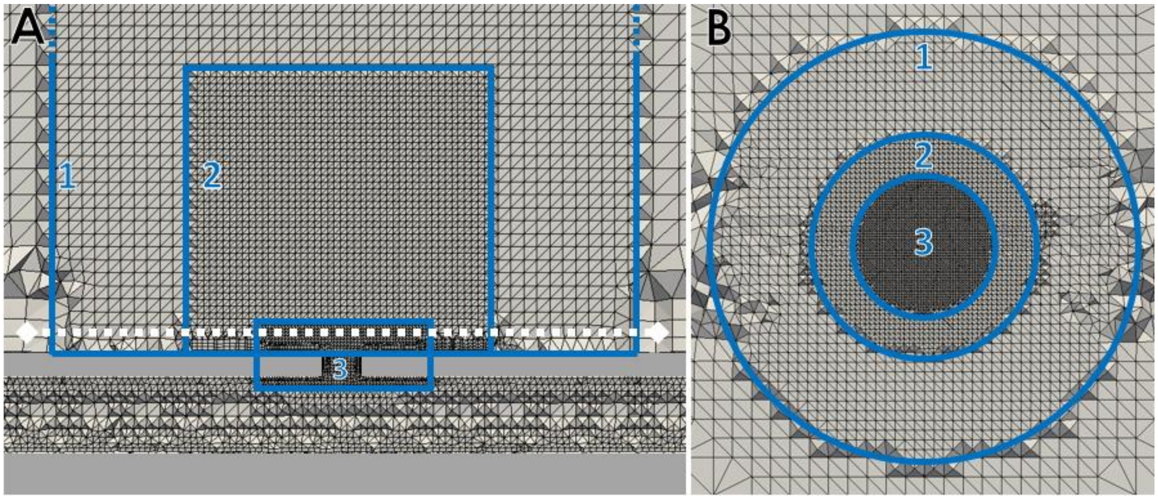

Fig. 4 Slice of computational mesh showing three critical successive cylindrical refinement regions: **A.** Front View (vertical slice across the midplane of the pipe) **B.** Top View (horizontal slice 1 mm above the center of the pipe, shown by the white dotted line in **A**).

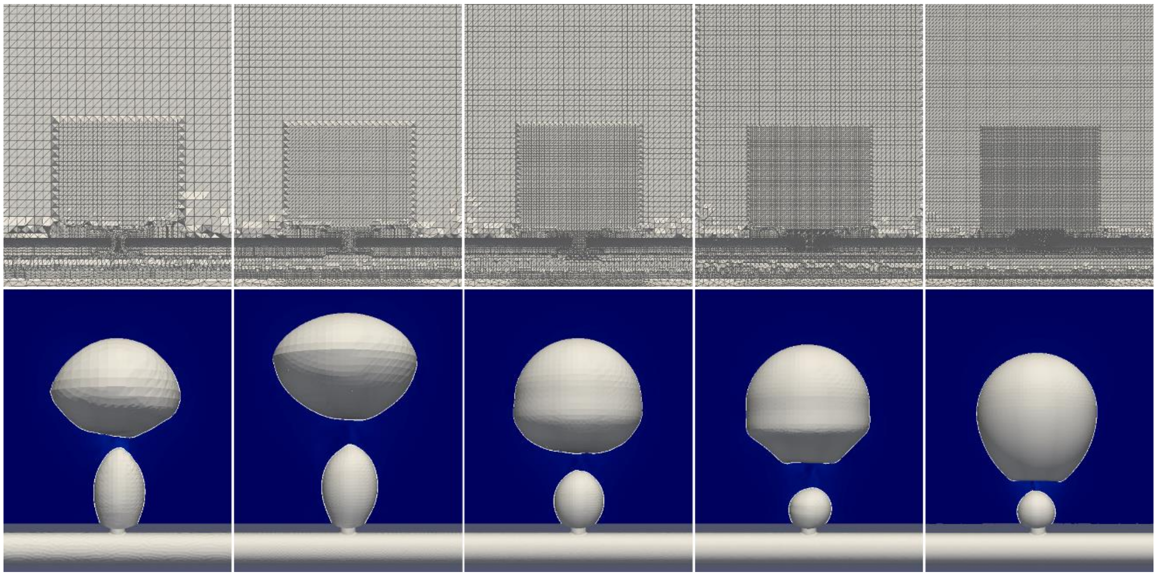

Fig. 5 First bubbles to depart at various mesh sizes going from coarsest (left) to finest (right), with detailed parameters present in Table 3.

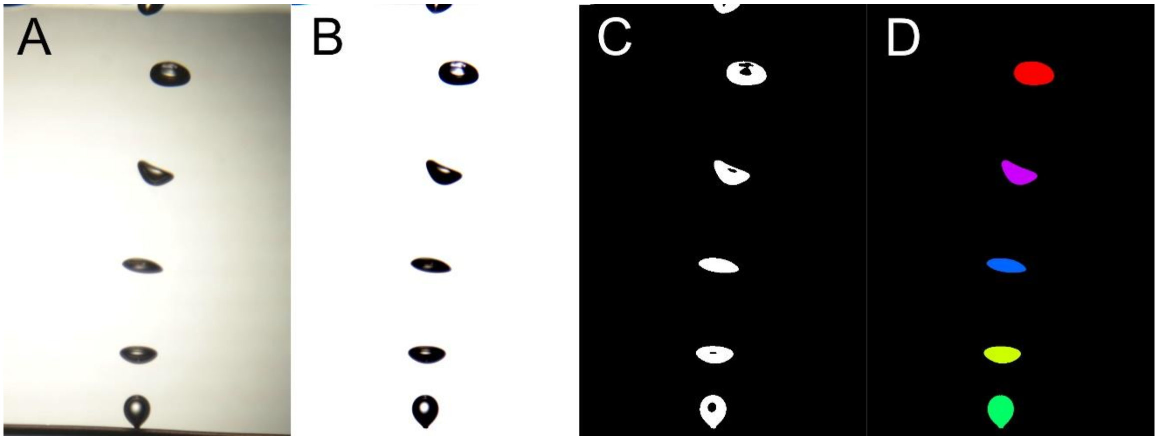

Fig. 6 Processing of experimental bubble trains with an air inflow of 50 mL/min. (A) The original image is subtracted from a biasing image to (B) extract only the bubbles from the image . (C) The processed image is converted to binary and inverted. (D) The “holes” are filled in by MatLab and colored to identify the bubble.

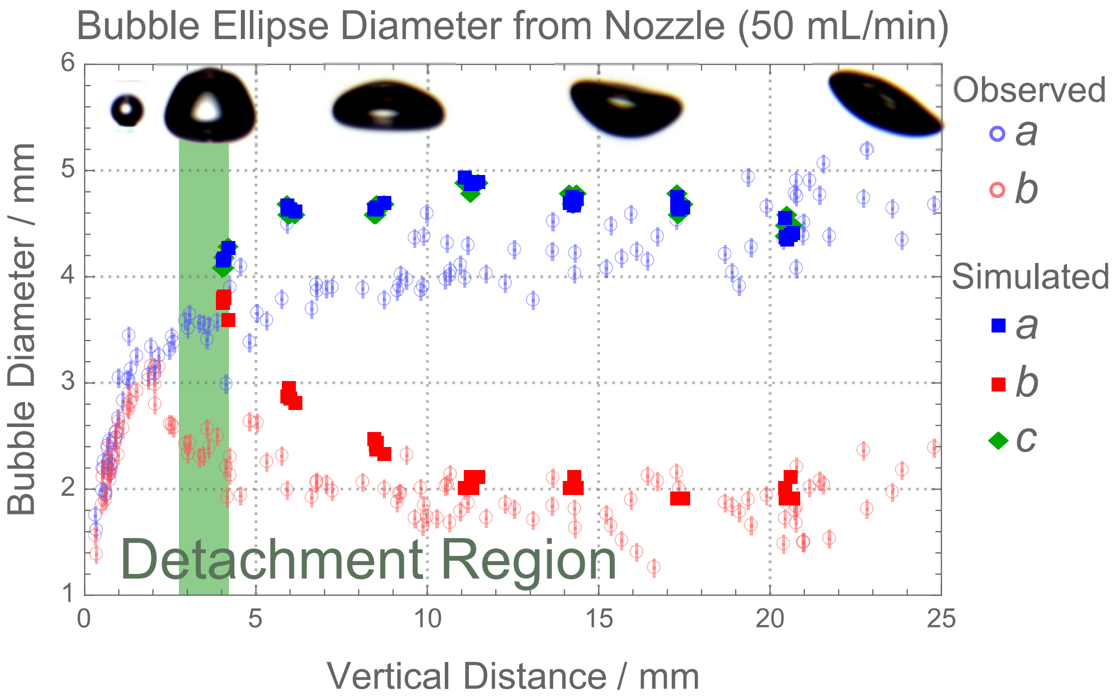

Fig. 7 Plot of major and minor diameters of the fitted ellipse of individual bubbles as a function of distance from the nozzle. The detachment region is highlighted in green. Bubble images are superimposed at the distances at which they appear in a single frame.

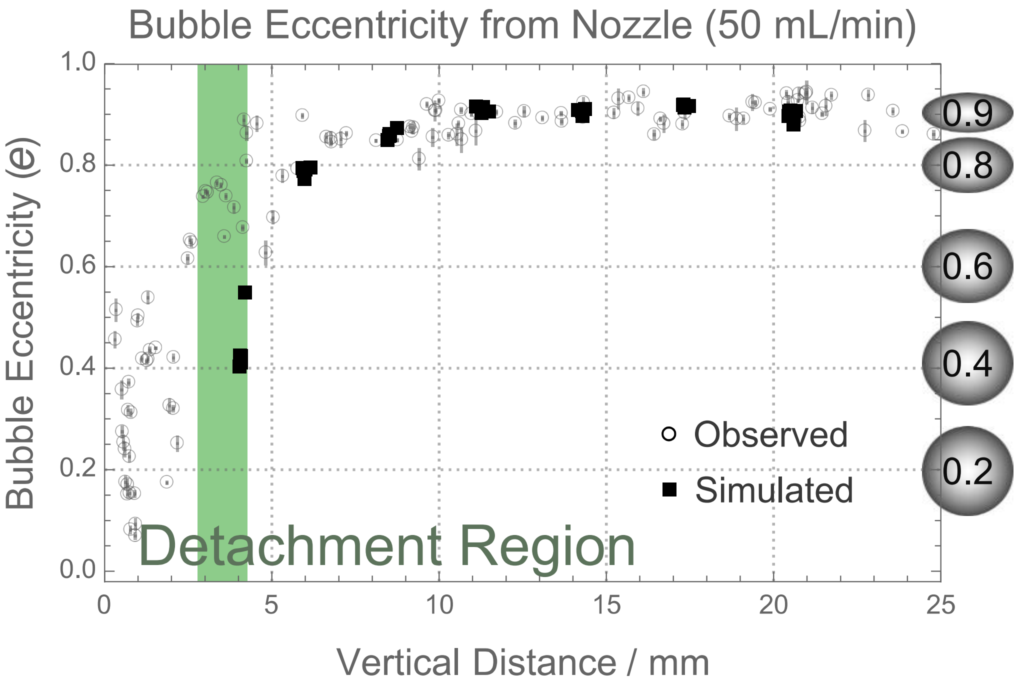

Fig. 8 Plot of the eccentricity of a fitted bubble as a function of vertical distance from the nozzle. The detachment region is highlighted in green. The shape of an ellipse is illustrated next to the corresponding eccentricity.

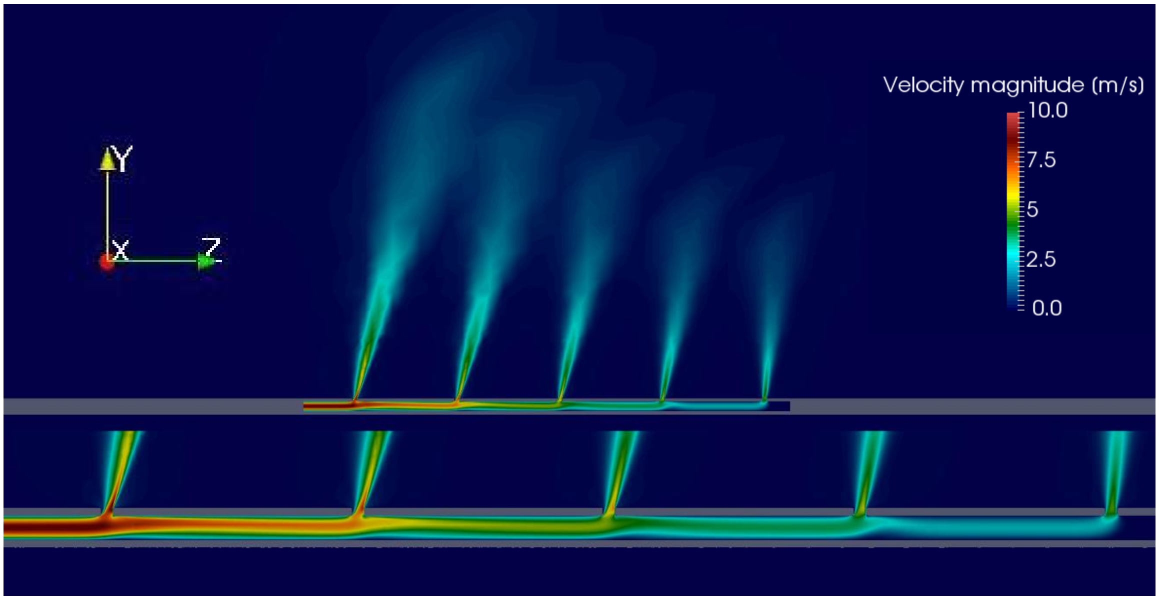

Fig. 9 Single phase flow distribution along the pipe

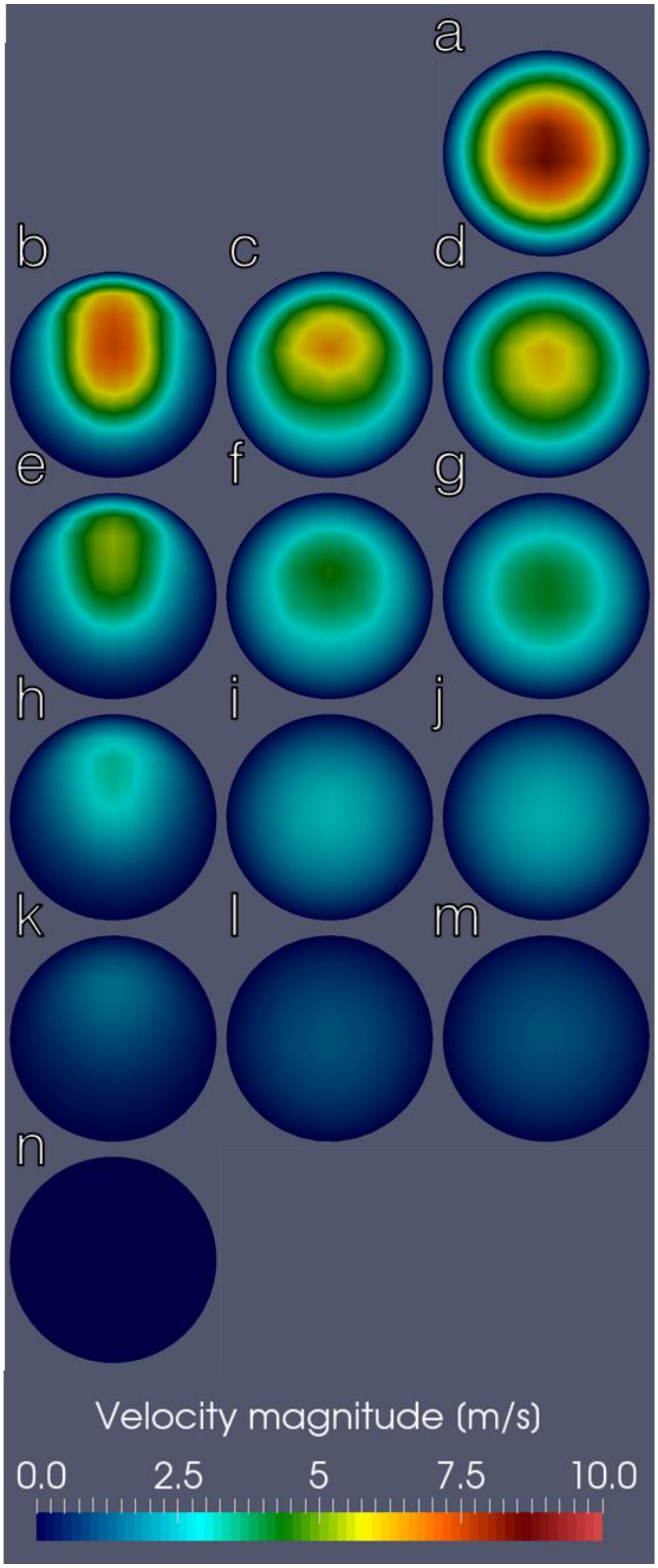

Fig. 10 Single phase flow distribution at various cross-sections. From top to bottom, left to right, the cross section positions are: z = -0.021, -0.019, -0.015, -0.011, -0.009, -0.005, -0.001, +0.001, +0.005, +0.009, +0.011, +0.015, +0.019, +0.021.

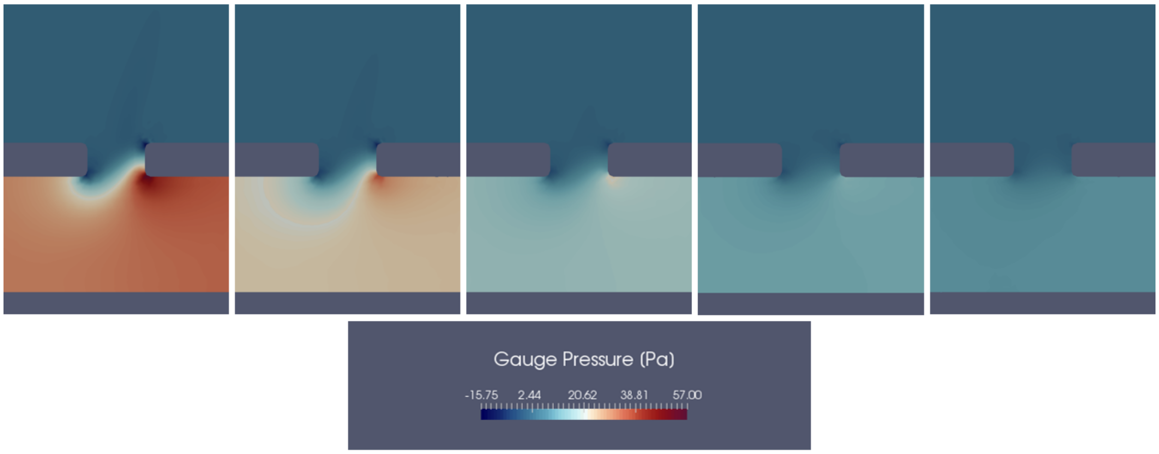

Fig. 11 Gauge pressure at each orifice during single phase flow

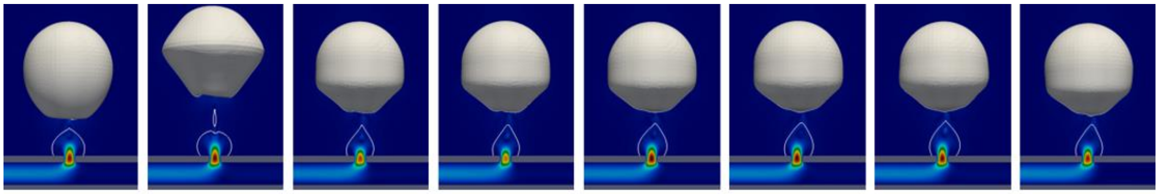

101.7 ms **157.6 ms** **205.4 ms** **254.5 ms** **303.1 ms** **351.9 ms** **400.4 ms** **448.1 ms**

Fig. 12 Bubble Departure for eight successive bubbles at 50 mL/min

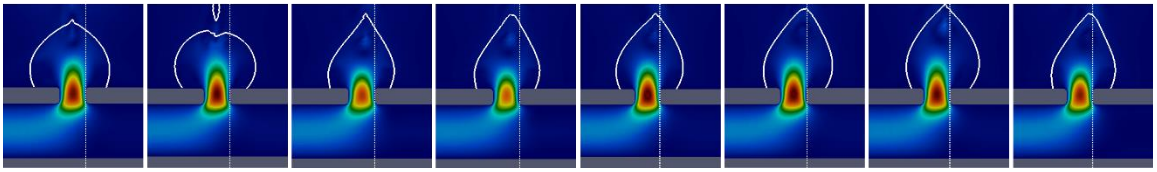

Fig. 13 Progressive leaning of remnant bubbles after departure events 1-8. The dotted line is parallel to the outermost edge of the nozzle in this plane. Each subsequent bubble progressively leans further to the right so while the tip of bubble #1 is nearly above the center of the nozzle, the tip of bubble #8 is just over the outermost edge of the nozzle.

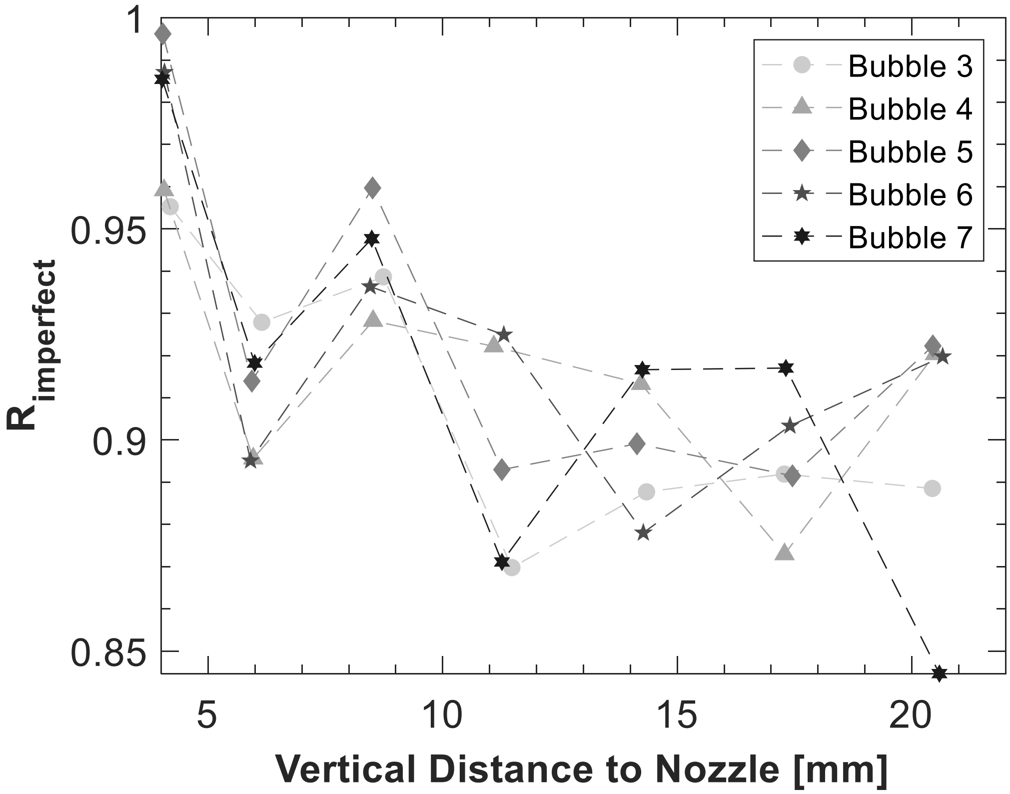

Fig. 14 Plot showing the decrease in alignment along cartesian axes during bubble ascension. Data points for each bubble are extracted every 10 milliseconds of simulation time.

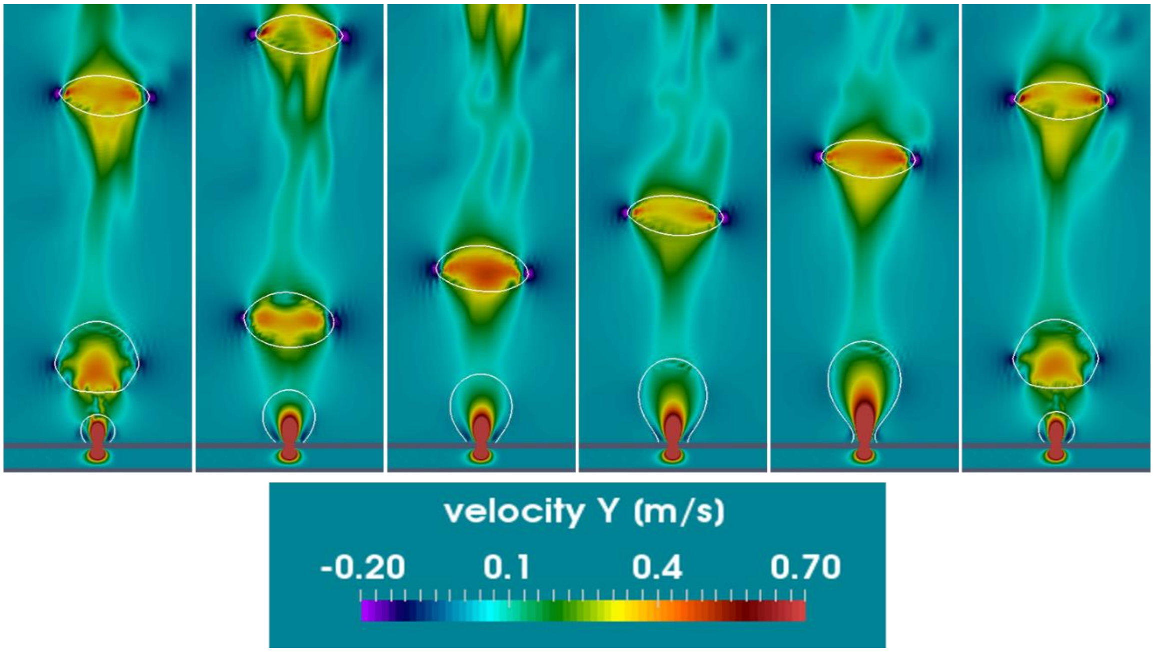

Fig. 15 Successive snapshots of a rising bubble. The velocity scale has been selected to highlight the local velocity changes within and around the bubble, thus the velocity gradient at the nozzle is not visible. This figure tracks the position of bubble #3 for 60 ms, with 10 ms passing in between each frame. Bubble # 2 is visible in the first 2 frames, and the formation and departure of bubble #4 can also be seen.

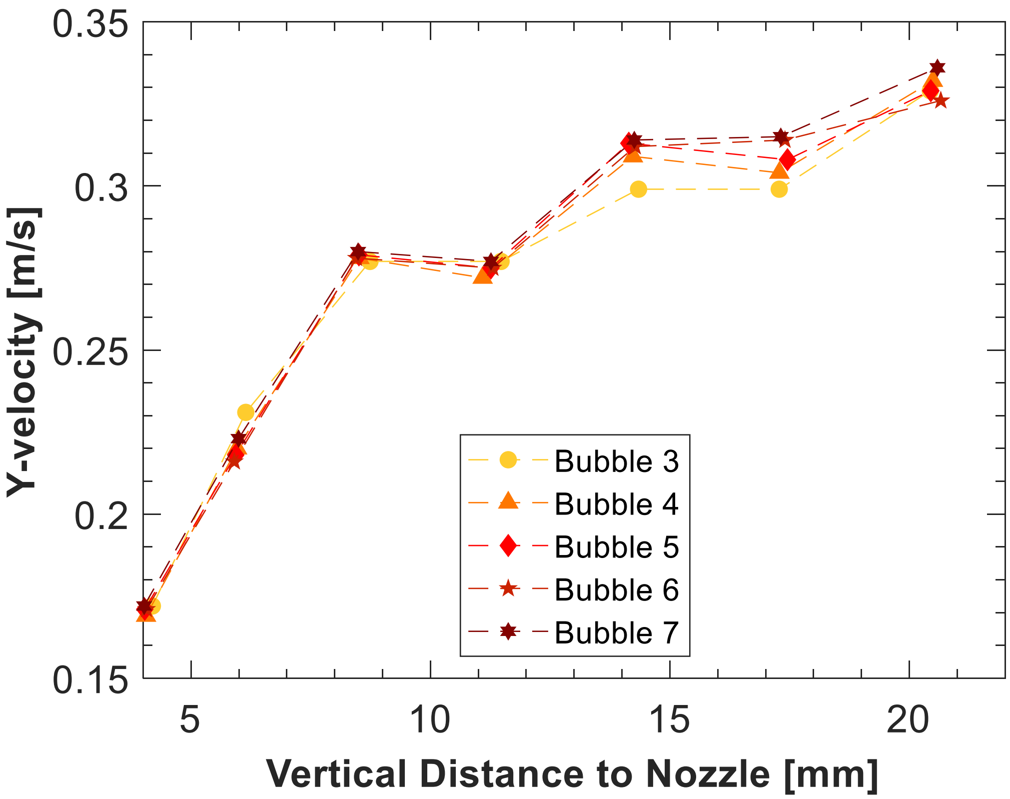

Fig. 16 Increase in bubble rise velocity during bubble ascent

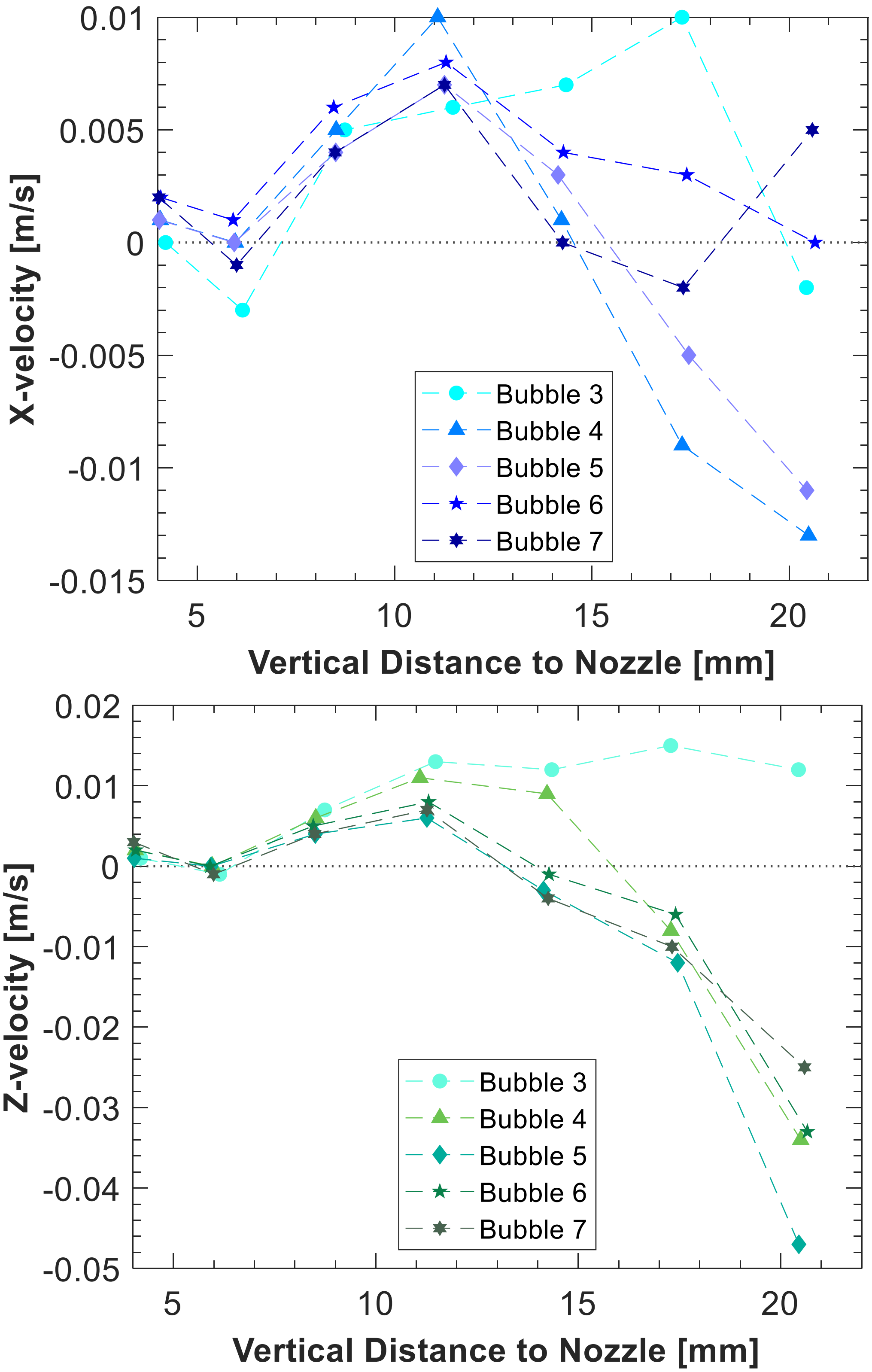

Fig. 17 Variation in tangential components of bubble velocity (X - blue and Z - green) about the nozzle center.

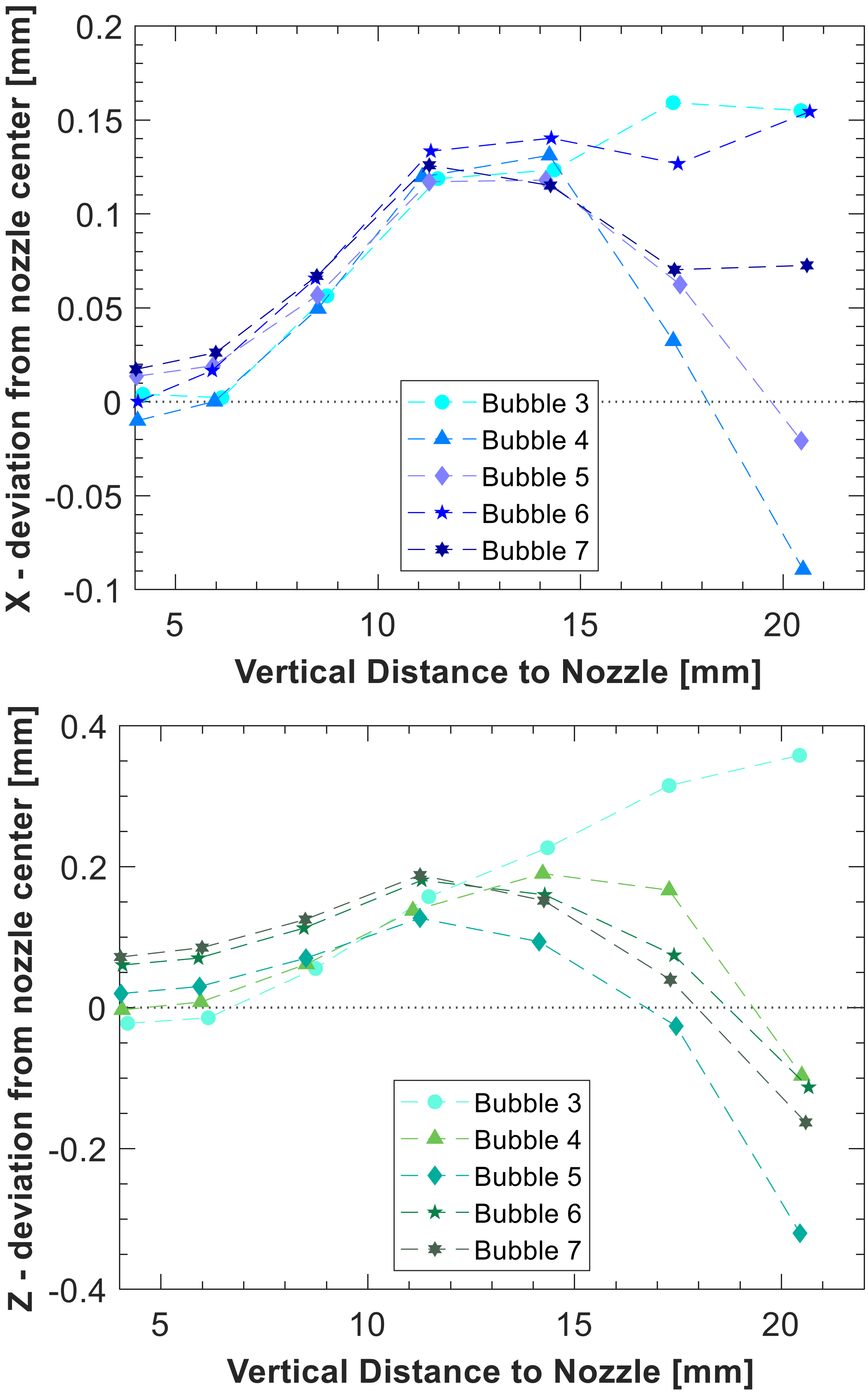

Fig. 18 Tangential deviation in bubble center of mass about the nozzle center.

Table Caption List

Table 1. Mesh Parameters

Parameter		Value
Total number of mesh elements		4,197,675
Elements across orifice		18
Elements across inner pipe		12
Region 1[a]	Elements across diameter	22
	Element Size	166.7 μm
	Vertical Height (above nozzle)	24,000 μm
Region 2[a]	Elements across diameter	42
	Element Size	83.3 μm
	Vertical Height (above nozzle)	3,400 μm
Region 3[a]	Elements across diameter	42
	Element Size	41.7 μm
	Vertical Height (above nozzle)	150 μm

[a] See Fig. 4

Table 2. Static and Dynamic Gas Volume Resolution based on Grid Volume

Relative Element Volume	Start Volume [mm^3]	Volume Added (Theory) [mm^3] [a]	Volume Added (Practice) [mm^3]	% Difference	Effective Flow Rate [mm^3/s]
400%	7.92	33.28	17.95	-46.1%	436.5
200%	7.96	37.89	27.00	-28.7%	578.5
100%	7.97	30.14	23.38	-22.4%	630.1
50%	7.98	27.82	21.96	-21.0%	644.7
25%	7.98	25.15	21.83	-13.2%	712.8

[a] Based on the inflow rate numerically measured near the inlet

Table 3. Effect of Mesh Resolution on Initial Bubble Formation

Relative Element Volume [a]	Bulk Element Edge Size [mm]	Relative Element Edge Size [a]	Detachment Time [ms]	First Bubble Volume [mm^3]	Number of Elements [b]
400%	8.46	1.59	54.20	24.23	653,933
200%	6.72	1.26	59.95	33.20	1,149,194
100%	5.33	1.00	50.36	31.58	1,937,951
50%	4.23	0.79	47.07	30.79	3,236,166
25%	3.36	0.63	43.73	30.67	5,751,417

[a] Relative to the main mesh used in this study (shown in Figure 4) in a truncated version of the domain described in Table 1.

[b] Due to the way the far-field elements were created (outside of the interest area), the number of elements does not scale exactly with relative element volume.

Table 4. Mesh Sensitivity of Initial Bubble Volume

	Mesh 1	**Mesh 2**	**Mesh 3**
Total Number of Elements	1,149,194	1,937,951	3,236,166
First Bubble Volume [mm^3]	33.2	31.6	30.8
Relative Error $\lvert\varepsilon\rvert$		4.88%	2.50%
GCI_{fine}		**5.79%**	**2.96%**
Order of Convergence, p		3.11	

Table 5. Spatial Data Generated by Bubble Imaging

position[a] [mm]	a[b] [mm]	b[c] [mm]	A_{meas}[d] [mm^2]	A_{calc}[e] [mm^2]	V_{calc}[f] [mm^3]	Ellipse Deviation [% difference]
(4.896 , 2.874)	1.544	1.281	6.113	6.212	12.788	1.601
(4.765 , 7.817)	1.923	1.064	6.331	6.428	16.477	1.513
(4.555 , 17.05)	2.005	0.914	5.758	5.758	15.388	0.864
(4.199 , 27.69)	2.292	0.825	5.722	5.941	18.156	3.687
(1.797, 38.55)	2.148	1.091	7.307	7.358	21.068	0.685

[a] ((z,y) positions from the first orifice)

[b] (major axis of ellipse imposed over bubble)

[c] (minor axis of ellipse imposed over bubble)

[d] (area calculated by pixel count of filled section of bubble)

[e] (area calculated for axes, $A=\pi ab$)

[f] (volume of bubble calculated assuming azimuthally symmetric oblate ellipsoid $V = (4/3)\, a \cdot A_{meas}$)

Table 6. Single Phase Flow Distribution Within the Pipe

z^a [m]	<v> [m/s]	Re	Flow Rate [ml/min]	Flow Rate [% of inflow]
-0.025	4.14	269.75	200.00	100.00%
-0.015	2.99	195.04	144.61	72.31%
-0.005	2.03	132.31	98.10	49.05%
+0.005	1.23	80.36	59.58	29.79%
+0.015	0.57	37.48	27.79	13.90%
+0.025	0.00	0.19	0.14	0.07%

[a] (where z = -0.02 is the position of the first orifice, and z = +0.02 is the position of the fifth orifice)

Table 7. Bubble Formation Characteristics at 50 mL/min

	Bubble Number							
	1	**2**	**3**	**4**	**5**	**6**	**7**	**8**
Formation Time [ms]	101.7	55.9	47.8	49.1	48.6	48.8	48.5	47.7
Expected Volume[a] [mm^3]	84.8	46.6	39.8	40.9	40.5	40.7	40.4	39.8
Simulation Volume [mm^3]	36.3	36.3	33.4	33.6	33.3	33.6	33.2	33.3
Mass defect (%)	-57%	-22%	-16%	-18%	-18%	-17%	-18%	-16%

[a] Assuming that all of the air inflow contributes to the volume of the bubble at the first orifice